The Journal of Chemical Physics

RESEARCH ARTICLE | JULY 16 2026

Vibrational carbon character analysis of astronomical PAHs

Kevin Fleming ; Vincent J. Esposito ; Ryan C. Fortenberry ; Mateus Quintano ; Elfi Kraka

J. Chem. Phys. 165, 034104 (2026)
https://doi.org/10.1063/5.0331629

The Journal of Chemical Physics ARTICLE pubs.aip.org/aip/jcp

Vibrational carbon character analysis of astronomical PAHs

Cite as: J. Chem. Phys. 165, 034104 (2026); doi: 10.1063/5.0331629
Submitted: 26 February 2026 • Accepted: 22 June 2026 •
Published Online: 16 July 2026

Kevin Fleming,[1] Vincent J. Esposito,[2] Ryan C. Fortenberry,[3] Mateus Quintano,[4] and Elfi Kraka[1,a)]

AFFILIATIONS

[1] Computational and Theoretical Chemistry Group (CATCO), Department of Chemistry, Southern Methodist University, 3215 Daniel Avenue, Dallas, Texas 75275-0314, USA
[2] Schmid College of Science and Technology, Chapman University, 1 University Drive, Orange, California 92866, USA
[3] Department of Chemistry and Biochemistry, University of Mississippi, 322 Coulter Hall, Oxford, Mississippi 38677, USA
[4] Department of Fundamental Chemistry, Federal University of Pernambuco, Recife, Pernambuco 50740-560, Brazil

[a)] **Author to whom correspondence should be addressed:** ekraka@mail.smu.edu

ABSTRACT

Emission features of astronomical spectra typically attributed to aromatic and aliphatic portions of polycyclic aromatic hydrocarbons (PAHs) should not be so clearly binned as previously ascribed. Vibrational carbon character analysis (VCCA) herein shows that the 3.4 μm aromatic infrared emission band (AIB), typically labeled as "aliphatic," possesses more than 45% non-aliphatic (i.e., aromatic) character for the test case of indene, the smallest astronomically detected PAH. Significant non-aliphatic character is seen as well for the 6.85 and 7.25 μm emission bands of indene, which are also considered to be markers of aliphaticity. VCCA predicts similar behavior for all three emission bands in the case of 2-ethynyltoluene, the proposed interstellar precursor of indene. Although the typical aromatic emission bands (i.e., 3.3 and 6.2 μm bands) exhibit slight aliphatic character for both indene and 2-ethynyltoluene, these bands are primarily aromatic. While these are only two example molecules, if significant character mixing occurs for the emission bands of most potential AIB carriers, current aliphatic/aromatic AIB attributions must be reconsidered.

I. INTRODUCTION

The aromatic infrared bands (AIBs) are emission features that have been observed in mid-IR spectra (3–20 μm) of many diverse astronomical environments, including planetary nebulae,[1] reflection nebulae,[2] HII regions,[3] ultraluminous infrared galaxies,[4] young stellar objects,[5] photodissociation regions,[6] post-AGB stars,[7] and protoplanetary disks[8,9] among others.[10,11] In the early 1980s, Leger and Puget[12] initially hypothesized that free-flying polycyclic aromatic hydrocarbons (PAHs) could serve as molecular carriers for AIBs, which were initially referred to as unidentified infrared emission (UIE) features.[13] The PAH hypothesis was further strengthened by Allamandola, Tielens, and Barker,[14,15] who describe how AIBs can arise from the IR emission of PAHs that are excited by UV photons in outer space—a cascade emission process that has since been extensively modeled in subsequent literature.[16–21] These molecules, however, were not detected in space until 2021, when McGuire *et al.*[22] discovered 1- and 2-cyanonapthalene in the Taurus molecular cloud (TMC-1) following the initial 2018 detection of benzonitrile toward the same astronomical source.[23] Since then, more PAHs have been detected,[24–32] with cyanocoronene being the largest PAH detected to date.[30] The current scientific consensus is that PAHs are the primary carriers of the AIBs, although there are other potential carriers as well.[13] Furthermore, none of the bands are exclusively attributed to the IR emission of a single PAH carrier; rather, they are attributed to the collective emission of multiple PAHs. The identities of these contributing PAH carriers remain uncertain; however, various studies have attempted to simulate the emission spectra of individual PAHs.[18,33–44] Andrews *et al.*[6] report that the emission of the most stable PAHs can account for the AIBs (i.e., the "grandPAH" hypothesis), while Rosenberg, Berné, and Boersma[45] find that the emission of at least 30 different PAHs—chosen at random—also accounts for these bands (i.e., the "multi-PAH" hypothesis). While both hypotheses are plausible, neither has been confirmed as of yet.

Although the specific PAH carriers that contribute to the AIBs await identification, the attribution of AIBs to the collective IR emission of multiple PAHs enables these bands to serve as spectral

probes of the molecules' general properties in various astronomical environments. Indeed, variations in the intensities, shapes, and peak positions of the AIBs across different environments have been attributed to generalized variations in PAH charge,[46,47] size,[48–50] molecular structure,[46,51–54] deuterium fractionation,[55–58] and carbon composition.[20,55,56,59–64] The evaluation of PAH carbon composition, in particular, has involved using AIBs to estimate the relative amounts of aromatic and aliphatic carbons in PAHs to better understand the underlying physical conditions that their chemical evolution in space indicates.[13] Certain AIBs are attributed exclusively to the deformation of aromatic C–H or C–C bonds (i.e., the 3.3 and 6.2 μm AIBs[10]), while others are attributed exclusively to the deformation of aliphatic C–H bonds (i.e., the 3.4, 6.85, and 7.25 μm AIBs[60,65–68]). On the basis of these attributions, the relative integrated emission intensity of aliphatic and aromatic AIBs (e.g., the $I_{3.4}/I_{3.3}$ intensity ratio) has been utilized to estimate the median PAH aliphatic/aromatic fraction, previously estimated by Yang and Li[64] to be 5.4%. However, a recent study of the interstellar PAH indene[24,25] and its proposed precursor 2-ethynyltoluene[69] by Esposito *et al.*[70] demonstrates that such AIB intensity ratios may actually be misleading due to the potential misattribution of the AIBs considered for these ratios. More specifically, the molecules' emission bands corresponding to the conventional aliphatic 3.4, 6.85, and 7.25 μm AIBs arise from vibrational transitions involving anharmonically coupled vibrational modes, and these coupled modes collectively describe the vibrational displacements (i.e., stretching, bending, and torsion) of *both* aliphatic and aromatic carbons.[70] In other words, due to this coupling, the conventionally described aliphatic AIBs may not be purely aliphatic. Rather, these AIBs may arise from anharmonic vibrational transitions that have what will be referred to hereafter as a mixed *vibrational carbon character* (VCC): the breakdown of a given set of vibrational displacements (e.g., those corresponding to a given vibrational transition) into displacements associated with ethynyl (sp), aromatic (sp^2), and aliphatic (sp^3) carbons.

This work serves to more precisely quantify the VCC of potential AIB carrier molecules' vibrational transitions—and, by extension, the VCC of their emission bands—to assess the veracity of the conventional aliphatic/aromatic attributions of the aforementioned AIBs. For this purpose, the vibrational carbon character analysis (VCCA) method is introduced herein. Utilizing both local vibrational mode theory (LVMT)[71,72] and second-order vibrational perturbation theory (VPT2),[73–77] VCCA effectively quantifies the VCC of each vibrational transition, thereby allowing for quantification of the VCC for potential AIB molecular carriers' emission bands, as well. Here, beginning with the theoretical and experimental data for indene and 2-ethynyltouene presented previously by Esposito *et al.*,[70] VCCA is applied to these two molecules. The VCC mixing predicted by VCCA for both molecules underscores the significance of considering the anharmonic coupling between vibrational modes in potential AIB carriers' vibrational transitions during the aliphatic/aromatic/ethynyl attribution of AIBs. More accurate attributions of AIBs, in turn, can refine the community's understanding not only of the molecular populations in observed regions but also of the astrophysical conditions in which such molecules can be found.

II. METHODOLOGY

A. LVMT: An overview

Normal vibrational mode analysis (Appendix A) is valuable for the study of electronic structure and chemical bonding of a given molecular system. However, normal vibrational modes are generally unable to represent the vibrational motions of individual bonds, bond angles, and dihedral angles due to their inherent delocalization.[78,79] To represent local vibrational motions, normal vibrational mode vectors must first be transformed into local vibrational mode vectors. For a given N-atom molecule with $N_{vib} = 3N - N_{tr}$ vibrational degrees of freedom (N_{tr} = 5 or 6 for linear or nonlinear molecules, respectively), these local mode vectors should be associated with a set of internal coordinates, $\{q_n, n = 1, \ldots, N_{vib}\}$, describing the molecule's bonds, bond angles, and dihedral angles. LVMT provides a prescription for the transformation of normal modes into local modes that meets this criterion. Konkoli and Cremer[80,81] demonstrated that each vector in $\{\mathbf{a}_n\}$, a set of local mode vectors associated with $\{q_n\}$, is expressed in normal coordinates as

$$\mathbf{a}_n = \frac{\mathbf{K}^{-1}\mathbf{d}_n^\dagger}{\mathbf{d}_n\mathbf{K}^{-1}\mathbf{d}_n^\dagger}, \tag{1}$$

where $\mathbf{d}_n$ is the nth row vector of the normal mode matrix $\mathbf{D}$ in internal coordinates, and $\mathbf{K}$ is the diagonal normal force constant matrix. Local mode vectors can be utilized to derive descriptors of bonds, bond angles, and dihedral angles, such as their local force constants, masses, and frequencies.[71,72,80,81] These properties of local modes are further discussed in Appendix B. In addition, each of the local mode vectors can undergo a coordinate transformation from normal coordinates to Cartesian coordinates,

$$\mathbf{a}_n^x = \mathbf{L}\mathbf{a}_n, \tag{2}$$

where $\mathbf{L}$ and $\mathbf{a}_n^x$ are the normal mode matrix and the local mode vector in Cartesian coordinates, respectively.[71,72,80,81] The transformed local mode vectors are suitable for the characterization of normal modes (CNM), an LVMT procedure that decomposes each delocalized normal mode into its local mode contributions from a non-redundant (i.e., linearly independent) set of N_{vib} local modes that is complete (i.e., the set spans the N_{vib}-dimensional space of normal modes).[71,82–85] The first step of the CNM procedure is computing the overlap between each Cartesian normal mode vector $\mathbf{l}_\mu$ ($\mu = 1, \ldots, N_{vib}$) and each Cartesian local mode vector $\mathbf{a}_n^x$. This overlap is given by

$$S_{n\mu} = \frac{\langle \mathbf{a}_n^x|\mathbf{H}|\mathbf{l}_\mu\rangle^2}{\langle \mathbf{a}_n^x|\mathbf{H}|\mathbf{a}_n^x\rangle\langle \mathbf{l}_\mu|\mathbf{H}|\mathbf{l}_\mu\rangle}, \tag{3}$$

where $\mathbf{H}$ is the Hessian matrix in Cartesian coordinates. With these overlap terms, the fractional contribution of a given local mode $\mathbf{a}_n^x$ to a normal mode $\mathbf{l}_\mu$ can be expressed as[71,82–85]

$$C_{n\mu} = \frac{S_{n\mu}}{\sum_{m=1}^{N_{vib}} S_{m\mu}}. \tag{4}$$

The contribution values given by Eq. (4) constitute the elements of the square ($N_{vib} \times N_{vib}$) CNM matrix, **C**. Each column of **C** represents the decomposition of a single normal mode $\mathbf{l}_\mu$ into contributions from each of the N_{vib} local modes; conversely, each row represents the contributions of a single local mode to each of the N_{vib} normal modes.

Over the past two decades, LVMT has been applied to molecular systems—in gas phase, solution, and protein environments—and periodic systems, with the aim of calculating the aforementioned properties of the systems' local modes and/or decomposing the systems' normal modes into their constituent local modes through CNM.[71,72] In this work, the atomic vibrational displacements of local mode vectors are also evaluated, as these displacements are directly utilized in the VCCA method, as described in Sec. II C. When evaluating the atomic displacements, the effects of atomic mass on the displacements must be accounted for. Thus, each $\mathbf{a}_n$ vector, which is mass-unweighted, must first be transformed into its mass-weighted analog $\tilde{\mathbf{a}}_n$, where the tilde denotes mass weighting. Once evaluated, the $\tilde{\mathbf{a}}_n$ vectors can undergo a coordinate transformation from normal coordinates to Cartesian coordinates, thereby yielding $\tilde{\mathbf{a}}_n^x$ vectors. These vectors are then utilized to evaluate the mass-weighted vibrational displacements of each atom for each local mode. The procedure utilized for the mass weighting of local modes and the subsequent transformation from normal coordinate space to Cartesian coordinate space is provided in Appendix C; a discussion of the invariance of the CNM matrix to local mode mass weighting is also provided therein.

B. Computational details

All geometry optimization and harmonic frequency calculations of indene and 2-ethynyltoluene are performed at the density functional theory (DFT) level of theory, with Gaussian 16.[86] DFT calculations utilized the B3LYP functional[87,88] and the N07D basis set,[89] which has been shown to more accurately treat anharmonicity in relatively large aromatic molecules.[90] The energy convergence threshold for the geometry optimization calculations was 1×10^{-12} E_h, and the numerical integration grid consists of 200 radial shells and 974 angular points per shell.

Once the equilibrium geometries of the molecules are determined, their corresponding quartic force fields (QFF) are computed at the same level of theory. A QFF is a fourth-order Taylor series approximation of the anharmonic potential energy surface around a given equilibrium geometry, which is expressed as

$$V = \frac{1}{2}\sum_{ij} F_{ij}\Delta_i\Delta_j + \frac{1}{6}\sum_{ijk} F_{ijk}\Delta_i\Delta_j\Delta_k + \frac{1}{24}\sum_{ijkl} F_{ijkl}\Delta_i\Delta_j\Delta_k\Delta_l, \quad (5)$$

where F_{ij}, F_{ijk}, and F_{ijkl} are the quadratic, cubic, and quartic force constants, respectively, while the Δ terms represent normal coordinate displacements from the equilibrium geometry.[91] Following a linear transformation of the QFF into Cartesian coordinates,[92] the QFF is then utilized to compute anharmonic frequencies and intensities through VPT2[73–77] as implemented in a modified version of the SPECTRO[93] program. In addition to calculating anharmonic frequencies and intensities, SPECTRO utilizes a polyad resonance matrix approach to VPT2 that accounts for the anharmonic coupling between vibrational modes (i.e., fundamentals, overtones, and combination bands) and quantifies the resulting redistribution of vibrational transition intensities across these modes.[19,94,95]

In parallel with the anharmonic VPT2 calculations, the LModeAGen protocol,[85] as implemented in the standalone LModeA package,[96] is utilized to generate a complete, non-redundant set of N_{vib} internal coordinates for each molecule. Once generated, this set of coordinates is corrected to account for the presence of any linear submolecules (e.g., the ethynyl group in 2-ethynyltoluene), as described in previous literature.[97] With the revised set of internal coordinates and the output data from the initial harmonic frequency calculations for both molecules, the set of associated mass-weighted Cartesian local mode vectors $\{\tilde{\mathbf{a}}_n^x\}$ and the CNM matrix (**C**) described in Sec. II A are computed.

The calculation of the mass-weighted Cartesian local mode vectors, the CNM matrix, and the VPT2 vibrational transition data, in particular, are essential to the VCCA method described in Sec. II C.

C. Vibrational carbon character analysis

Figure 1 outlines the workflow of the VCCA method to evaluate the VCC breakdown (i.e., the percent vibrational ethynyl, aromatic, and aliphatic carbon character) of AIB carrier emission bands. In other words, the ultimate aim is to determine the relative contributions of vibrational modes involving ethynyl, aromatic, and aliphatic carbons to each band. The workflow of the VCCA method begins with an initial geometry optimization and harmonic frequency calculation for the molecule of interest at any suitable level of theory. For AIB carriers such as PAHs, DFT is a suitable and heavily used[98–108] level of theory, since higher-accuracy coupled-cluster methods for optimization/frequency calculations of PAHs are currently computationally intractable due to their size. Previously detected interstellar PAHs range in size from 17 atoms (i.e., indene[24,25]) to 37 atoms (i.e., cyanocoronene[30]), while even larger species are predicted to exist in space.[109,110] After the initial optimization and harmonic frequency calculations are completed, the VPT2 and LVMT calculations discussed in Sec. II B are performed.

1. Local mode character breakdown

Once the local mode vectors ($\{\tilde{\mathbf{a}}_n^x\}$) are determined from the LVMT calculations, the VCC breakdown of each of these vectors can be evaluated. As previously mentioned, each local mode is associated with an internal coordinate described by N atoms, where N = 2 (bonds), 3 (bond angles), or 4 (dihedrals). This set of N atoms can be partitioned as

$$N = N_C + N_R = N_{Et} + N_{Ar} + N_{Al} + N_R, \quad (6)$$

where $N_C = N_{Et} + N_{Ar} + N_{Al}$ and the N_{Et}, N_{Ar}, and N_{Al} terms denote the number of atoms contributing exclusively to either the vibrational ethynyl, aromatic, or aliphatic carbon character of the local mode, respectively, while N_R denotes the remaining number of atoms described by the coordinate. As a first step in evaluating N_{Et}, N_{Ar}, and N_{Al}, each carbon in the mode's associated internal coordinate is classified as ethynyl (sp), aromatic (sp^2), or aliphatic (sp^3). For example, considering the Al–Ar carbon stretching local mode of indene shown in Fig. 1, it is evident that $N_{Al} = N_{Ar} = 1$, since one of the stretching carbon atoms is aromatic and its counterpart is aliphatic, as labeled in the figure.

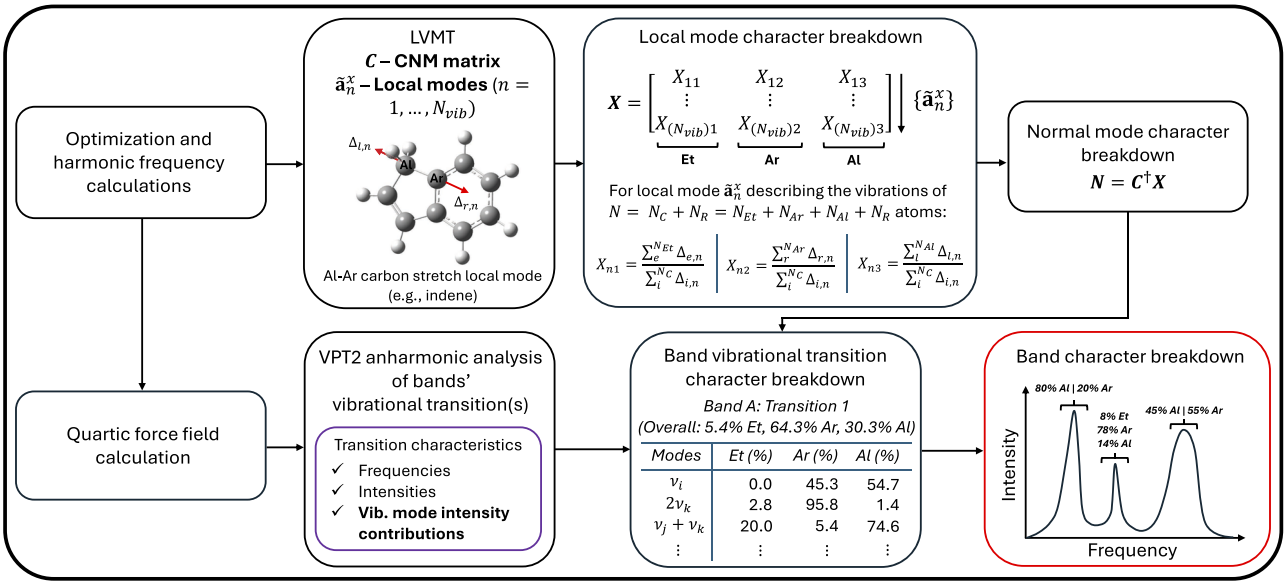

FIG. 1. Workflow of the VCCA method for calculating the VCC of AIB carrier emission bands. Et, Ar, and Al refer to ethynyl, aromatic, and aliphatic, respectively. See the text for further explanation of the workflow.

While the partitioning of N is straightforward when considering an internal coordinate describing only carbon atoms, the internal coordinates must be considered where non-carbon atoms, especially hydrogens and nitrogens, are present. There are three special cases of such internal coordinates:

1. The internal coordinate describes a non-carbon atom that is not bonded to any carbon atom within the coordinate (e.g., N–H bond). Here, the associated local mode motion of the non-carbon atom is not associated with the motion of any type of carbon. Therefore, this non-carbon atom is assigned to the set of atoms described by N_R.
2. The internal coordinate describes a non-carbon atom and one bonded carbon (e.g., C–H or C≡N bonds). In this case, the local vibrational motion of the non-carbon atom is associated only with the motion of the bonded carbon (e.g., aliphatic/aromatic/ethynyl C–H stretch or ethynyl C≡N stretch). Therefore, the non-carbon atom can be assigned to the same set as the bonded carbon (i.e., N_{Et}, N_{Ar}, or N_{Al}).
3. The internal coordinate describes a non-carbon atom and multiple bonded carbon atoms [e.g., $\angle$(C–N–C) bond angle or τ(C–N–C–C) dihedral angle]. There are two subcases to consider here. In the first subcase, the internal coordinate describes a non-carbon atom and two or more bonded carbon atoms that belong to *two or more different sets* of carbon atoms [e.g., $\angle$(C_1–N–C_2) bond angle for which C_1 is aromatic and C_2 is aliphatic]. For a non-carbon atom bonded to such carbon atoms, its local vibrational motion is not exclusively associated with the motion of a single type of carbon. Therefore, the non-carbon atom cannot be assigned exclusively to one of the sets described by N_{Et}, N_{Ar}, and N_{Al} and would instead be assigned to the set described by N_R—similar to case 1. In the second subcase, the internal coordinate describes a non-carbon atom and bonded carbon atoms that all belong to *the same set* of carbon atoms (e.g., if C_1 and C_2 from the first subcase example were both aromatic instead). In this scenario, the non-carbon atom's local vibrational motion is exclusively associated with the motion of one type of carbon atom. Hence, the non-carbon atom can be assigned to the same set as its neighboring identical carbons—similar to case 2.

The partitioning of N for a given internal coordinate with a non-carbon atom first requires a careful evaluation of the number of carbons bonded to the non-carbon atom that are also *described by the internal coordinate*. This number is the sole criterion used to distinguish between cases 1-3, and the overall number of carbons bonded to the non-carbon atom is not necessarily the same value. For instance, indole-3-acetaldehyde, a biomolecule that can be derived from the polycyclic aromatic nitrogen-containing hydrocarbon (PANH) indole,[111] contains a single nitrogen atom embedded in its five-membered ring that is bonded to two aromatic carbons (Fig. 2): C_2 and C_9. In this structure, however, bonds, angles, and dihedral angles can be identified describing N_1 and only one of its two bonded carbons, such as the N_1–C_2 bond, the $\angle$(N_1–C_2–C_3) bond angle, and the τ(N_1–C_2–C_3–C_4) dihedral angle. Since these particular coordinates only describe one of N_1's bonded carbons (i.e., C_2), they can be classified as instances of case 2 rather than case 3. Although at first glance counting only the N_1-bonded carbons that are described by these internal coordinates (i.e., one carbon) instead of all the N_1-bonded carbons (i.e., two carbons) may seem erroneous, each local mode associated with an internal coordinate describes the localized vibrational motion of *only* the

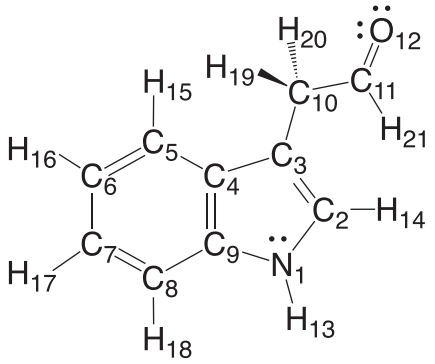

FIG. 2. Labeled chemical structure of indole-3-acetaldehyde.

N atoms described by the coordinate. Thus, the atoms not described by the three coordinates, including the C_9 atom bonded to N_1, are not associated with the local vibrational motion of N_1 corresponding to these coordinates. This compartmentalization of vibrational motions would not be true, however, if the N partitioning scheme was applied to normal modes instead of local modes, since the vibrations of the former can be delocalized throughout the entire molecular system—that is, they are not strictly associated with a single bond, bond angle, or dihedral angle.

Internal coordinates can, of course, also describe multiple non-carbon atoms with differing numbers of carbon bonds, thereby meeting the criteria for more than just one of the three special cases. Returning to the example of indole-3-acetaldehyde, the dihedral angle $\tau(C_9–N_1–C_2–H_{14})$ ($N = 4$) can be considered, which describes a hydrogen bonded to a single carbon (case 2) and a nitrogen bonded to two carbons (case 3). The prescriptions for cases 2 and 3 can be applied separately to the hydrogen and nitrogen, respectively. Since C_2 is aromatic, H_{14} belongs to the set described by N_{Ar} based on the prescription for case 2. Similarly, since both C_2 and C_9 are aromatic, N_1 also belongs to the set described by N_{Ar} based on the prescription for case 3. Thus, the partition of N for the dihedral is given simply as $N = N_{Ar} = 4$. Table S1 of the supplementary material lists the partitioning of N for a subset of indole-3-acetaldehyde's internal coordinates.

After N has been partitioned for all N_{vib} local mode vectors, the results of the partitioning can be directly utilized to evaluate the VCC of each vector. The local mode character breakdown matrix, $\mathbf{X}$, with dimensions of $N_{vib} \times 3$ (Fig. 1), contains the character of the local mode vectors. The nth row of $\mathbf{X}$ contains the character breakdown of local mode $\tilde{\mathbf{a}}_n^x$, with elements,

$$X_{n1} = \frac{\sum_e^{N_{Et}} \Delta_{e,n}}{\sum_i^{N_c} \Delta_{i,n}}, \tag{7}$$

$$X_{n2} = \frac{\sum_r^{N_{Ar}} \Delta_{r,n}}{\sum_i^{N_c} \Delta_{i,n}}, \tag{8}$$

and

$$X_{n3} = \frac{\sum_l^{N_{Al}} \Delta_{l,n}}{\sum_i^{N_c} \Delta_{i,n}}, \tag{9}$$

where $\Delta_{e,n}$, $\Delta_{r,n}$, and $\Delta_{l,n}$ denote the local mode vector displacements of each atom belonging to the sets described by N_{Et}, N_{Ar}, and N_{Al}, respectively, while $\Delta_{i,n}$ denotes the displacement of each atom belonging to the overall set described by N_c. The relative displacements of the partitioned atoms are quantified by the displacement ratios of X_{n1}, X_{n2}, and X_{n3}, which together sum up to unity since $N_c = N_{Et} + N_{Ar} + N_{Al}$. These displacement ratios represent the relative vibrational contributions of the partitioned atoms to the vibrational motion of the local mode. Thus, X_{n1}, X_{n2}, and X_{n3} denote the vibrational ethynyl, aromatic, and aliphatic carbon character of $\tilde{\mathbf{a}}_n^x$, respectively.

2. Normal mode character breakdown

Through CNM, the relative contributions of different local modes to a given normal mode can be quantified. For a given normal mode $\mathbf{l}_\mu$, the contributions of each constituent local mode [$C_{n\mu}$, Eq. (4)] sum up to unity,

$$\sum_{n=1}^{N_{vib}} C_{n\mu} = 1. \tag{10}$$

The character of the normal mode can therefore be evaluated as the weighted sum of the characters of the local modes, with their corresponding $C_{n\mu}$ terms acting as weighting coefficients. As discussed in Appendix C, the mass weighting of the Cartesian local modes does not affect the CNM matrix $\mathbf{C}$. With this in mind, a $N_{vib} \times 3$ normal mode character breakdown matrix, $\mathbf{N}$, is defined and contains the elements,

$$N_{\mu c} = \sum_{n=1}^{N_{vib}} C_{n\mu} X_{nc}. \tag{11}$$

Equation (11) can be recast in matrix form as

$$\mathbf{N} = \mathbf{C}^\dagger \mathbf{X}, \tag{12}$$

where $\mathbf{N}$ is analogous to $\mathbf{X}$, with each row of the former describing the character of an individual normal mode.

3. Band character breakdown

Each emission band of an AIB carrier corresponds to one or more IR absorption bands. Furthermore, each IR absorption band corresponds to one or more vibrational transitions, and each of these transitions arises from anharmonic coupling between various vibrational fundamentals, overtones, and combination bands. Thus, the VCC of an emission band can be evaluated by analyzing the VCC of its corresponding absorption bands, which can be derived from the VCC of the absorption bands' corresponding transitions. In addition, the VCC of each transition can be determined from the VCC for each of its corresponding vibrational modes. Hence, a bottom–up approach can be employed to compute the emission bands' VCC.

First, the characters of the fundamentals, overtones, and combination bands contributing to each transition are evaluated. The $\mathbf{N}$ matrix quantifies the character of normal modes (i.e., fundamentals). Since each overtone is associated with only one fundamental, the character of the overtone is the same as that of the fundamental.

Combination bands, however, involve two different fundamentals; their character is the unweighted average of the characters of the two fundamentals. Based on these considerations, for a vibrational transition involving N_M vibrational modes, an $N_M \times 3$ vibrational mode character breakdown matrix, **M**, is defined. For a mode m $(m = 1, \ldots, N_M)$ that is a fundamental ν_i or its corresponding overtone $2\nu_i$,

$$M_{mc} = N_{ic}. \tag{13}$$

If m is a combination band $\nu_j + \nu_k$, then

$$M_{mc} = \frac{1}{2}(N_{jc} + N_{kc}). \tag{14}$$

Once **M** is evaluated, the character of each transition can be evaluated. Here, the fractional intensity contributions of each mode to each transition, computed previously with VPT2, come into play. More specifically, for an absorption band with N_T vibrational transitions, a $N_T \times 3$ band transition character breakdown matrix, **T**, is defined and contains elements,

$$T_{tc} = \sum_{m}^{N_M} \omega_{m,t} M_{mc}, \tag{15}$$

where $\omega_{m,t}$ is the VPT2 fractional intensity contribution of mode m to transition t $(t = 1, \ldots, N_T)$. The use of the $\omega_{m,t}$ terms in Eq. (15) as weighting coefficients directly accounts for the anharmonic coupling between the modes involved in the transition.

Once **T** has been evaluated, the character of each absorption band can be determined by computing the weighted VCC average of the band's transitions, using the normalized VPT2 anharmonic intensities of each transition as weights. For an emission band with N_A corresponding absorption bands, a $N_A \times 3$ band character breakdown matrix, **A**, is defined and contains elements,

$$A_{ac} = \frac{\sum_t^{N_T} I_{t,a} T_{tc}}{\sum_t^{N_T} I_{t,a}}, \tag{16}$$

where $I_{t,a}$ is the intensity of transition t assigned to absorption band a $(a = 1, \ldots, N_A)$.

Finally, the character of each emission band can be determined by computing the weighted VCC average of the emission band's corresponding absorption band(s). This averaging procedure uses the normalized intensities of each corresponding absorption band as weights. For N_E emission bands, a $N_E \times 3$ band character breakdown matrix, **E**, is defined with elements,

$$E_{ec} = \frac{\sum_a^{N_A} I_{a,e} A_{ac}}{\sum_a^{N_A} I_{a,e}}, \tag{17}$$

where $I_{a,e}$ is the intensity of absorption band a corresponding to emission band e $(e = 1, \ldots, N_E)$. In this work, the experimental absorption band intensities previously evaluated by Esposito *et al.*[70] are utilized for the values of $I_{a,e}$. However, experimental data are not required for this step. In the absence of experimental spectra, VPT2 anharmonic intensities for the absorption bands can be utilized instead.

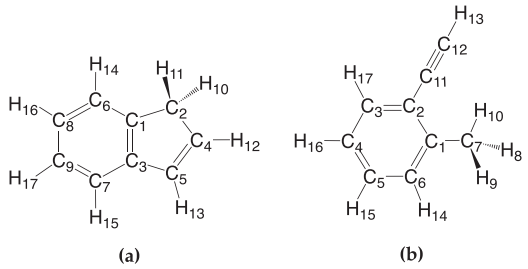

FIG. 3. Labeled chemical structures of (a) indene and (b) 2-ethynyltoluene.

III. RESULTS AND DISCUSSION

Figure 3 depicts the labeled chemical structures of indene and 2-ethynyltoluene. The experimental absorption spectra and the computed anharmonic line spectra of the two molecules are shown in Figs. 4 and 5. Vibrational transition assignments to each absorption band by Esposito *et al.*[70] use the results of the aforementioned anharmonic VPT2 calculations. Based on these vibrational transition assignments, the VCCA method is applied to each molecule to compute the VCC breakdown of their absorption and emission bands given in Tables I–IV. Tables S2–S11 of the supplementary material provide the partitioning of N, local mode VCC breakdown, normal mode VCC breakdown (i.e., for normal modes ν_1–ν_{45}), absorption band transition intensity contributions, and absorption band transition VCC breakdown for indene and 2-ethynyltoluene, respectively. The present discussion centers around the VCC breakdown for the molecules' conventionally ascribed aliphatic 3.4, 6.85, and 7.25 μm emission bands and the conventional aromatic 3.3 and 6.2 μm emission bands. Overall, the VCCA results indicate that these bands are not purely aromatic or aliphatic, respectively, for these two molecules. The 3.4, 6.85, and 7.25 μm emission bands, in particular, show significant, non-negligible aromatic character—in stark contrast to their conventional aliphatic attributions.

A. Band VCC breakdown: Indene

1. Dissection of the 3.4, 6.85, and 7.25 μm conventional aliphatic bands

The 3.4 μm emission band corresponds to six neighboring absorption bands: **G**, **H**, **I**, **J**, **K**, and **L** (Fig. 4). Bands **G**, **H**, **J**, **K**, and **L** have >70% aromatic character (Table I) due to the influence of several highly aromatic combination bands (Table S5, supplementary material), whose consituent fundamentals are mostly aromatic (Table S4, supplementary material). Band **I**, on the other hand, has ~90% aliphatic character, which can be understood by considering the character of its two transitions at 2900.9 and 2902.6 cm^{-1} (Table S6, supplementary material). The 2900.9 cm^{-1} transition mainly derives its near-pure aliphatic character from the ν_7 fundamental, associated with the antisymmetric stretches of the aliphatic C_2–H_{10} and C_2–H_{11} bonds. The 2902.6 cm^{-1} transition is also primarily aliphatic due to the ν_8 fundamental, which is associated with the symmetric stretches of the aforementioned aliphatic bonds. Despite the pronounced aliphaticity of **I**, however, the competing aromatic character contributions of **G**, **H**, **J**, **K**, and **L** result in the ~45% aromatic character of the 3.4 μm emission band

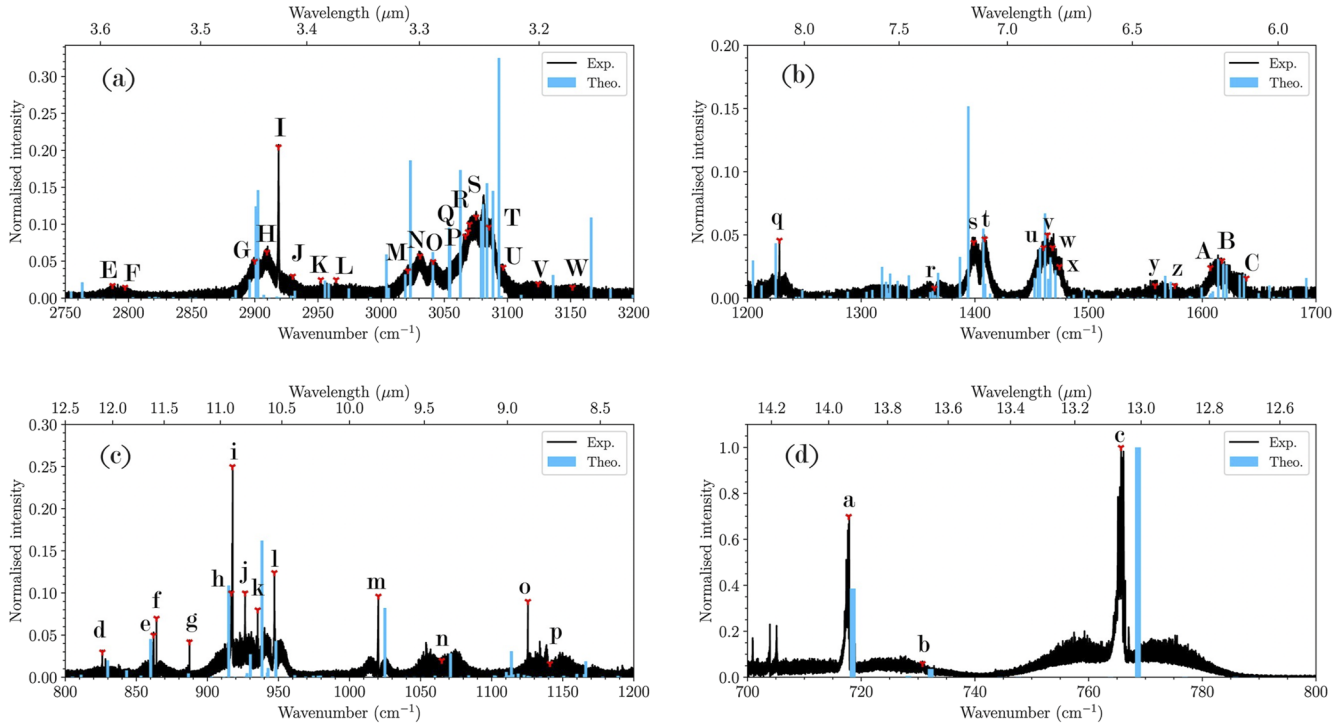

FIG. 4. Experimental absorption spectrum of indene (black) along with its computed anharmonic line spectra (blue). Vibrational transitions for bands **a**–**W**, originally assigned by Esposito *et al.*, are shown in Table S5 of the supplementary material. Esposito *et al.*, Mon. Not. R. Astron. Soc. **535**, 3239 (2024). Copyright 2024 Author(s), licensed under a Creative Commons Attribution 4.0 License.

(Table II). Thus, contrary to convention, this emission band possesses a non-negligible aromatic character and cannot be labeled purely as aliphatic, at least for this one example.

In addition, the 6.85 and 7.25 μm emission bands are primarily *aromatic*, not aliphatic, as evidenced by the characters of their corresponding absorption bands. The 6.85 μm band corresponds to absorption bands **u**, **v**, **w**, and **x**, which are all mostly aromatic, since they stem from highly aromatic transitions involving combination bands and overtones with >70% aromatic character. In the case of the 7.25 μm emission band, however, the corresponding absorption bands **r**, **s,** and **t** cause the emission band to have a more pronounced—albeit still minor—aliphatic character compared to its 6.85 μm counterpart. While **r** and **t** are >80% aromatic, **s** is nearly half-and-half in terms of its aliphatic–aromatic character divide. The reason for this near-even divide of character can be traced back to the variations in the intensities and character breakdowns of the absorption band's three transitions at 1386.9, 1393.6, and 1394.2 cm^{-1}. Although the first two transitions are >80% aromatic, the third transition is ~60% aliphatic due to the strongly aliphatic ν_{14} fundamental, associated with the out-of-plane bending of the C_2–H_{10} and C_2–H_{11} bonds. This third transition also has an intensity that is more than 70% of the sum of all three transitions' intensities. Thus, the character contribution of the third transition significantly outweighs the contributions of the first two, leading to the half-and-half aliphatic-aromatic character divide of band **s**. Nonetheless, the dominant aromatic characters of **r** and **t** result in the primarily aromatic character of the 7.25 μm band.

2. 3.3 and 6.2 μm conventional aromatic bands

The 3.3 μm emission band corresponds to three absorption bands: **M**, **N**, and **O**, which each have >95% aromatic character. The absorption bands' transition(s) involve the highly aromatic ν_4–ν_6 fundamentals associated with the C–H stretching motions of aromatic carbons C_6–C_9, as well as highly aromatic combination bands involving modes ν_9–ν_{13} (e.g., $\nu_9 + \nu_{12}$). These combination bands are associated with the delocalized in-plane skeletal distortions in the underlying carbon ring structure, which is mainly composed of aromatic carbons. However, the distortions also involve the displacements of the aliphatic C_2 atom and its bonded hydrogens, thereby contributing to the trace amounts of aliphatic character (i.e., ~3 – 4%) observed for **M**, **N**, and **O**. Consequently, although the 3.3 μm emission band corresponding to these three absorption bands is primarily aromatic, it is not *purely* aromatic.

In addition, the higher frequency absorption bands in the range of 3050–3200 cm^{-1} (~3.25 – 3.15 μm) are also mainly aromatic with the interesting exception of band **U**, which is ~70% aliphatic. This

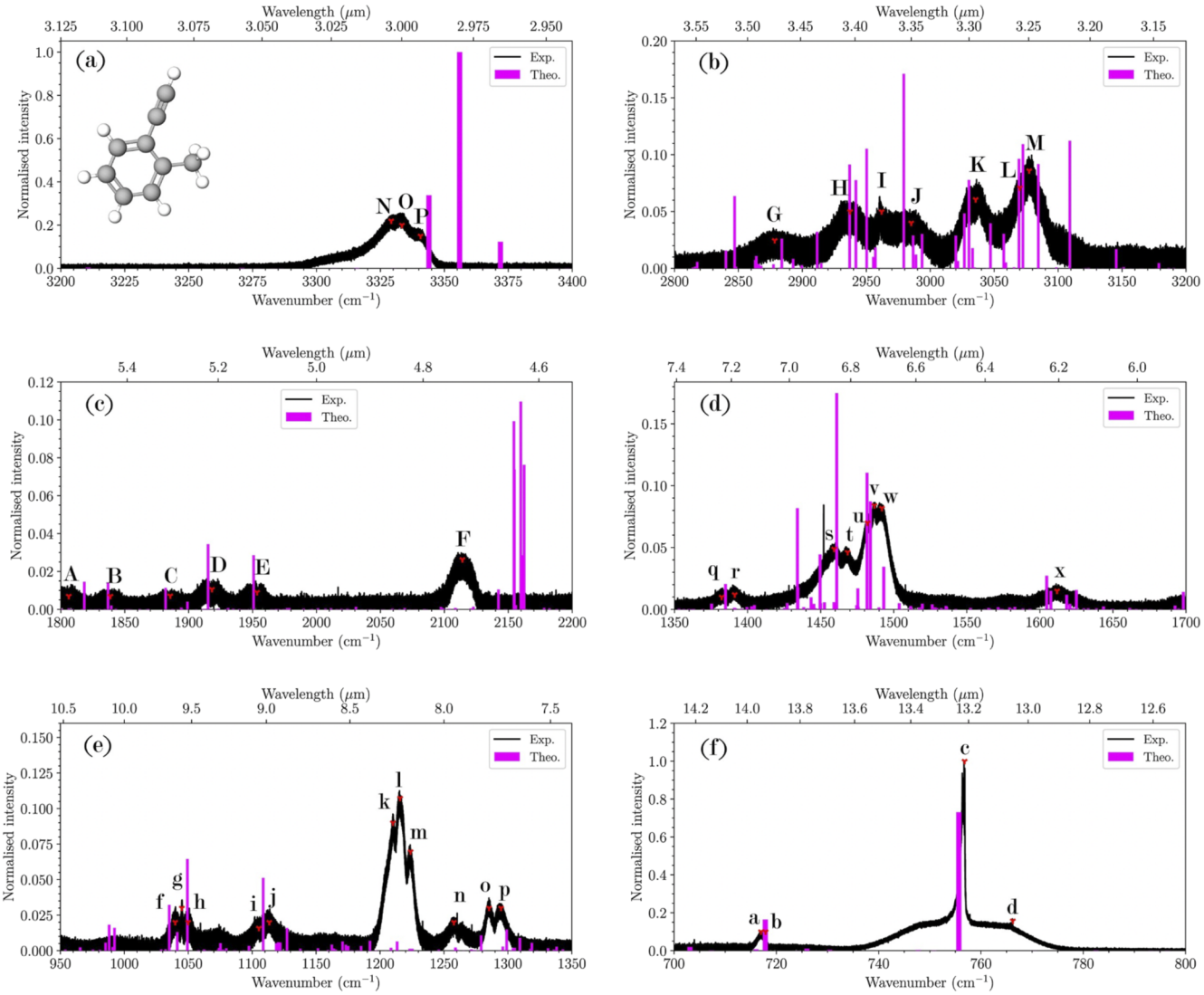

FIG. 5. Experimental absorption spectrum of 2-ethynyltoluene (black) along with its computed anharmonic line spectra (pink). Vibrational transitions for bands **a**–**P**, originally assigned by Esposito *et al.*, are shown in Table S10 of the supplementary material. Esposito *et al.*, Mon. Not. R. Astron. Soc. **535**, 3239 (2024). Copyright 2024 Author(s), licensed under a Creative Commons Attribution 4.0 License.

band's single transition at 3095.2 cm^{-1} derives almost all of its intensity and character from combination band $\nu_7 + \nu_{45}$. One of the two modes involved in this combination band, ν_7—the aforementioned antisymmetric aliphatic C–H stretching fundamental—is the most significant contributor of aliphatic character to **U**. Conversely, ν_{45}, which is highly delocalized and involves the out-of-plane bending motions of all the aromatic carbons and their bonded hydrogens, is mostly responsible for the remaining ~30% aromatic character of **U**. These results suggest that any emission bands between ~3.25–3.15 μm, while still being primarily aromatic, possess aliphatic character as well.

The slightly aliphatic character of conventional aromatic emission bands is also evident upon examination of absorption bands **y**, **z**, **A**, **B**, and **C**, corresponding to the 6.2 μm emission band. These absorption bands have ~6% – 20% aliphatic character, leading to the 6.2 μm band's ~15% aliphatic character. **y** and **z** each have a single transition, and their singular transitions have $\gtrsim$ 85% character contributions from combination bands that are ~6 – 16% aliphatic. **A** has three transitions at 1606.7, 1607.6, and 1609.3 cm^{-1} that have prominent character contributions from combination bands that are ~9 – 25% aliphatic. **C** also exhibits a share of aliphatic character similar to **A** due to the former's two transitions at 1632.9 and

TABLE I. VCC breakdown of indene's absorption bands **a**–**W**, shown in Fig. 4. Et, Ar, and Al refer to ethynyl, aromatic, and aliphatic VCC, respectively.

Band	Et (%)	Ar (%)	Al (%)
a	0.0	82.1	17.8
b	0.0	81.4	18.6
c	0.0	85.6	14.3
d	0.0	64.0	35.9
e	0.0	85.6	14.4
f	0.0	93.3	6.6
g	0.0	76.7	23.2
h	0.0	63.6	36.4
i	0.0	83.0	17.0
j	0.0	85.5	14.5
k	0.0	59.9	40.0
l	0.0	63.4	36.6
m	0.0	98.5	1.5
n	0.0	91.2	8.8
o	0.0	19.3	80.7
p	0.0	76.2	23.8
q	0.0	72.5	27.5
r	0.0	83.6	16.4
s	0.0	51.1	48.9
t	0.0	84.6	15.4
u	0.0	87.4	12.6
v	0.0	86.2	13.7
w	0.0	92.6	7.3
x	0.0	74.7	25.3
y	0.0	93.9	6.1
z	0.0	84.5	15.4
A	0.0	80.9	19.0
B	0.0	88.7	11.2
C	0.0	80.0	20.0
D	0.0	98.6	1.4
E	0.0	53.5	46.5
F	0.0	32.7	67.2
G	0.0	83.7	16.3
H	0.0	75.4	24.6
I	0.0	12.9	87.1
J	0.0	94.5	5.4
K	0.0	87.7	12.2
L	0.0	70.1	29.9
M	0.0	97.1	2.9
N	0.0	95.8	4.1
O	0.0	97.1	2.9
P	0.0	97.7	2.3
Q	0.0	98.9	1.1
R	0.0	97.5	2.5
S	0.0	97.4	2.6
T	0.0	96.4	3.5
U	0.0	31.1	68.9
V	0.0	96.4	3.6
W	0.0	97.1	2.9

TABLE II. VCC breakdown of indene's conventional aromatic (i.e., 3.3 and 6.2 μm) and aliphatic (i.e., 3.4, 6.85, 7.25 μm) emission bands, each of which corresponds to the absorption bands shown in Fig. 4. Et, Ar, and Al refer to ethynyl, aromatic, and aliphatic VCC, respectively.

Emission band (μm)	Absorption bands	Et (%)	Ar (%)	Al (%)
3.3	**M–O**	0.0	96.6	3.4
3.4	**G–L**	0.0	45.5	54.5
6.2	**y, z, A–C**	0.0	84.8	15.1
6.85	**u–x**	0.0	86.3	13.6
7.25	**r–t**	0.0	69.6	30.4

1636.9 cm^{-1}, which have prominent character contributions from combination bands that are ~11 – 27% aliphatic. **B** has less aliphatic character than **A** and **C**, since its three transitions at 1614.0, 1618.5, and 1621.3 cm^{-1} primarily involve fundamentals and combination bands that have ~5 – 15% aliphatic character. The combination bands that helped contribute to the aliphaticity of the five absorption bands involve various highly delocalized modes (e.g., ν_{18}, ν_{24}, ν_{30}, ν_{37}, ν_{40}, etc.). Due to their strong delocalization, these modes describe the vibrational displacements of aliphatic C_2 and its bonded hydrogen atoms alongside those of the aromatic carbons (e.g., skeletal distortions), thereby resulting in the combination bands' partial aliphaticity.

B. Band VCC breakdown: 2-ethynyltoluene

1. 3.4, 6.85, and 7.25 μm conventional aliphatic bands

Like indene, 2-ethynyltoluene also has a 3.4 μm emission band with non-negligible (~43%) aromatic character (Table IV)—once again at odds with its conventional aliphatic attribution. The two corresponding absorption bands are **H** and **I** (Fig. 5). Band **H** is ~65% aliphatic, and it has three transitions at 2936.9, 2941.8, and 2950.2 cm^{-1} (Table S10, supplementary material). The first two of these transitions demonstrate nearly a half-and-half split in their aromatic-aliphatic character divide, with only ~1% ethynyl character (Table S11, supplementary material). They act as the strongest aromatic character contributors to **H** despite the competing aliphatic influence of the third transition, which is ~90% aliphatic due to the purely aliphatic ν_7 fundamental—associated with the antisymmetric stretching of the aliphatic C_7–H_8 and C_7–H_{10} bonds of 2-ethynyltoluene's methyl group. Band **I** only shows one transition at 2957.1 cm^{-1} that, similar to the 2936.9 and 2941.8 cm^{-1} transitions of **H**, is nearly half-and-half in terms of its aromatic–aliphatic character divide. This divide is almost entirely due to a single combination band, $\nu_{11} + \nu_{16}$, which is ~53% aromatic and ~47% aliphatic. Together, **H** and **I** contribute to the 3.4 μm emission band's highly mixed character breakdown for this molecule, as well.

A different type of character mixing is observed for what is actually a predominantly aromatic 6.85 μm emission band corresponding to bands **s** and **t**. Band **s** has ~29% ethynyl and ~3% aliphatic character; hence, the vibrational displacements of the 2-ethynyltolunene's ethynyl group—and not those of its methyl group—predominantly contribute to the non-aromatic character of this band. More specifically, the character breakdown of **s**'single

TABLE III. VCC breakdown of 2-ethynyltoluene's absorption bands **a**–**P**, shown in Fig. 5. Et, Ar, and Al refer to ethynyl, aromatic, and aliphatic VCC, respectively.

Band	Et (%)	Ar (%)	Al (%)
a	18.0	77.7	4.3
b	1.9	90.0	8.1
c	2.6	96.6	0.8
d	57.3	31.6	11.0
e	2.5	88.3	9.1
f	0.3	21.9	77.7
g	38.9	55.2	5.9
h	6.4	88.8	4.8
i	7.9	77.6	14.5
j	3.7	26.3	69.9
k	11.6	78.0	10.4
l	6.8	85.5	7.6
m	20.4	68.5	11.1
n	24.7	69.5	5.8
o	5.1	87.0	7.9
p	8.0	86.7	5.2
q	5.0	33.7	61.3
r	0.6	11.9	87.5
s	28.8	68.0	3.1
t	2.3	73.4	24.3
u	10.6	82.8	6.6
v	15.7	79.4	4.8
w	3.7	53.2	43.0
x	10.1	82.3	7.5
y	1.7	95.5	2.8
z	3.1	95.3	1.6
A	0.4	95.0	4.6
B	0.1	97.7	2.1
C	0.1	58.0	41.9
D	0.1	97.6	2.2
E	0.0	100.0	0.0
F	24.4	66.7	8.9
G	2.0	68.7	29.3
H	0.8	36.1	63.2
I	0.2	50.8	48.9
J	0.4	26.3	73.3
K	1.1	82.4	16.5
L	2.6	84.2	13.2
M	0.6	96.4	3.1
N	64.0	31.8	4.2
O	85.5	12.6	1.9
P	59.7	33.1	7.3

transition at 1449.5 cm^{-1} reveals that ~90% of the transition's character is derived from a combination band involving modes ν_{17} and ν_{43}. While ν_{17} primarily describes the delocalized displacements of aromatic carbons, ν_{43} primarily describes the in-plane bending of the ethynyl group. The ethynyl character contribution of this in-plane bending mode is mostly responsible for the ~29% ethynyl character of **s**. Unlike band **s**, however, band **t** possesses significantly stronger aliphatic character (~24%) than ethynyl character (~2%)

TABLE IV. VCC breakdown of 2-ethynyltoluene's conventional aromatic (i.e., 3.3 and 6.2 μm) and aliphatic (i.e., 3.4, 6.85, and 7.25 μm) emission bands, corresponding to the absorption bands shown in Fig. 5. Et, Ar, and Al refer to ethynyl, aromatic, and aliphatic VCC, respectively.

Emission band (μm)	Absorption band(s)	Et (%)	Ar (%)	Al (%)
3.3	**K**	1.1	82.4	16.5
3.4	**H**, **I**	0.5	43.5	56.1
6.2	**x**	10.1	82.3	7.5
6.85	**s**, **t**	17.0	70.4	12.5
7.25	**q**, **r**	2.8	22.8	74.4

due to the dominant character contribution of fundamental mode ν_{13}, associated with the bending of the methyl group's C–H bonds. Yet, **s** and **t** partially counterbalance each other's characters, leading to the 6.85 μm band's more balanced ethynyl-aliphatic character divide.

The 7.25 μm emission band of 2-ethynyltoluene, corresponding to bands **q** and **r**, is the most aliphatic of the three conventional aliphatic emission bands, although it also possesses ~25% non-aliphatic character. Band **q** is ~34% aromatic and 5% ethynyl in character. Nearly all of this non-aliphatic character is derived from combination band $\nu_{24} + \nu_{41}$, which describes, among other motions, the in-plane bending of the aromatic C–H bonds as well as those of the ethynyl group. In strong contrast to **q**, however, **r** is ~90% aliphatic; the latter's strong aliphaticity is derived from a ~90% aliphatic fundamental, ν_{16}, which describes the bending motion of the methyl C–H bonds. Yet, the significant non-aliphatic character of **q** competes with the aliphaticity of **r**, causing the 7.25 μm emission band to have non-negligible non-aliphatic character as well.

2. 3.3 and 6.2 μm conventional aromatic bands

As previously discussed in the case of indene, absorption bands **M**, **N**, and **O**, associated with the 3.3 μm emission band, are >95% aromatic. For 2-ethynyltoluene, however, the only absorption band associated with the emission band, **K**, showcases a greater aliphatic character than indene's **M**, **N**, and **O**. This behavior leads to the ~16% aliphatic character of the 3.3 μm band. Examining **K**'s four transitions at 3020.0, 3026.7, 3030.2, and 3033.1 cm^{-1}, five combination bands contribute to the partially aliphatic character of **K**: $\nu_7 + \nu_{45}$, $\nu_{10} + \nu_{12}$, $\nu_{10} + \nu_{15}$, $\nu_{11} + \nu_{13}$, and $\nu_{11} + \nu_{15}$. The modes involved in these combination bands describe, most notably, the stretching, bending, and twisting of the aliphatic methyl C–H bonds. Compared to the methylene group in indene, the methyl group in 2-ethynyltoluene not only has an additional aliphatic C–H bond but also an additional conformational flexibility. As such, the latter aliphatic group has more vibrational freedom (i.e., more possible vibrational motions) than the former. This difference may explain the greater involvement of partially aliphatic vibrational modes for **K** compared to indene's bands **M**, **N**, and **O**, resulting in **K**'s greater partial aliphatic character. This unique property also potentially explains why the 3.3 μm band of 2-ethynyltoluene, while still being

primarily aromatic, has a more pronounced aliphatic character than its indene counterpart.

Lastly, the absorption band **x** corresponding to the 6.2 μm emission band is strikingly similar in aromatic character to **K**. Unlike **K**, however, the non-aromatic character in **x** is not mostly aliphatic but, rather, is ~10% ethynyl and ~8% aliphatic. A comparison of the transitions involving **x** at 1604.7, 1607.5, 1618.4, and 1625.0 cm^{-1} explains why this band contains more pronounced ethynyl character. The 1604.7 and 1607.5 cm^{-1} transitions have the same two primary contributing modes: ν_{10} and $\nu_{13} + \nu_{43}$. While ν_{10} mainly describes the delocalized vibrations of the aromatic and aliphatic carbons and their bonded hydrogens, $\nu_{13} + \nu_{43}$ additionally describes the in-plane bending of the ethynyl group, among other motions. Together, these two vibrational modes confer both ethynyl and aliphatic character to their transitions and, by extension, to **x** as well. The 1618.4 and 1625.0 cm^{-1} transitions, on the other hand, are ~90% aromatic. As a result, they slightly counteract the non-aromatic character contributions of the 1604.7 and 1607.5 cm^{-1} transitions to **x**. Nonetheless, the latter transitions ultimately contribute to the emission band's ~18% non-aromatic character.

IV. CONCLUSION

For indene and 2-ethynyltoluene, the conventional aliphatic 3.4, 6.85, and 7.25 μm emission bands have significant non-aliphatic character ranging from ~25 – 87%, in agreement with and quantitatively expanding upon the findings from Esposito *et al.*[70] In addition, while the conventional aromatic 3.3 and 6.2 μm emission bands are indeed primarily aromatic, they are not purely aromatic due to smaller amounts of non-aromatic character ranging from ~3 – 18%. For the vibrational transitions of each molecule, the anharmonic coupling between vibrational modes results in VCC mixing that prevents emission bands from being exclusively associated with the vibrational displacements of only one type of carbon. Thus, the VCCA results presented in this work strongly call for a detailed examination of the VCC mixing of other potential AIB carriers as well. If significant VCC mixing occurs for most carriers, the attribution of certain AIBs as being purely aliphatic/aromatic needs to be reconsidered. Furthermore, if these attributions are erroneous, then the use of AIB intensity ratios to evaluate the PAH aliphatic/aromatic fraction also warrants reconsideration.

Additionally, the VCCA results prompt a myriad of questions concerning the connection between VCC mixing and various properties of PAHs. For example, since larger PAHs have more vibrational states than smaller PAHs, does their greater number of vibrational states imply stronger anharmonic coupling between these states, leading to greater VCC mixing for larger PAHs? Do the overall charge and spin multiplicity of PAHs also influence VCC mixing? In addition, do processes such as deuterium fractionation, inclusion of heteroatoms (e.g., nitrogen), or the functionalization of PAHs with different aromatic/aliphatic/alkynyl functional groups play a role as well? As demonstrated herein, VCCA can serve as a promising means to address these questions in future work. Answering such questions would enrich the community's understanding of how the VCC of PAH emission bands may evolve during the evolution of their associated interstellar/circumstellar environments, such as low-mass stellar systems, where significant PAH formation, destruction, and chemical alteration may take place.[62] Such insights would greatly facilitate the astrochemical and astrophysical interpretation of the IR observational data of these environments.

SUPPLEMENTARY MATERIAL

See the supplementary material for the partitioning of N for indole-3-acetaldehyde, followed by the partitioning of N, local mode VCC breakdown, normal mode VCC breakdown, absorption band transition intensity contributions, and absorption band transition VCC breakdown for indene and 2-ethynyltoluene.

ACKNOWLEDGMENTS

K.F. and E.K. thank Dr. Filippo Bodo for his valuable suggestions during this study, the SMU O'Donnell Data Science and Computing Center for providing excellent computational resources, the SMU Moody School of Graduate and Advanced Studies for their support through the SMU Moody Graduate Fellowship, and the NASA Texas Space Grant Consortium (TSGC) for their support through the NASA TSGC Graduate Fellowship. M.Q. thanks Pernambuco Research Foundation (FACEPE) for Postdoctoral Fellowship No. BFP-0039-1.06/24.

AUTHOR DECLARATIONS

Conflict of Interest

The authors have no conflicts to disclose.

Author Contributions

Kevin Fleming: Conceptualization (equal); Formal analysis (equal); Methodology (equal); Validation (equal); Writing – original draft (equal); Writing – review & editing (equal). **Vincent J. Esposito**: Conceptualization (equal); Formal analysis (equal); Methodology (equal); Writing – review & editing (equal). **Ryan C. Fortenberry**: Conceptualization (equal); Formal analysis (equal); Methodology (equal); Writing – review & editing (equal). **Mateus Quintano**: Methodology (equal); Writing – review & editing (equal). **Elfi Kraka**: Conceptualization (equal); Funding acquisition (lead); Methodology (equal); Supervision (lead); Writing – review & editing (equal).

DATA AVAILABILITY

The data that support the findings of this study are available within the article and its supplementary material.

APPENDIX A: NORMAL VIBRATIONAL MODE ANALYSIS

For a given N-atom molecule, there are $N_{vib} = 3N - N_{tr}$ normal vibrational degrees of freedom (N_{tr} = 5 or 6 for linear or nonlinear

molecules, respectively). Within the Born–Oppenheimer approximation,[112] the N_{vib}-dimensional potential energy surface (PES) of the molecule is considered. The Taylor expansion of the PES at a given point $\mathbf{x}$ with respect to a stationary point $\mathbf{x}_0$ can be expressed as

$$V(\mathbf{x}) = V(\mathbf{x}_0) + \sum_{i}^{N}\sum_{\alpha}^{3}\left(\frac{\partial V}{\partial u_{i\alpha}}\right)_{\mathbf{x}_0} u_{i\alpha} + \frac{1}{2!}\sum_{ij}^{N}\sum_{\alpha\beta}^{3}\left(\frac{\partial^2 V}{\partial u_{i\alpha}\partial u_{j\beta}}\right)_{\mathbf{x}_0} u_{i\alpha}u_{j\beta} + \frac{1}{3!}\sum_{ijk}^{N}\sum_{\alpha\beta\gamma}^{3}\left(\frac{\partial^3 V}{\partial u_{i\alpha}\partial u_{j\beta}\partial u_{k\gamma}}\right)_{\mathbf{x}_0} u_{i\alpha}u_{j\beta}u_{k\gamma} + \ldots, \tag{A1}$$

where $\alpha, \beta, \gamma, \ldots$ each refer to the three Cartesian directions and $i, j, k, \ldots$ each refer to the N atoms; together, they denote the 3N Cartesian atomic displacement terms defining $\mathbf{x}$ (i.e., $u_{i\alpha}$, $u_{j\beta}, u_{k\gamma}, \ldots$). The PES minima at $\mathbf{x}_0$ can be set to zero [i.e., $V(\mathbf{x}_0) = 0$], and the first partial derivatives of the PES at $\mathbf{x}_0$ are equal to zero $\left[\text{i.e., } \left(\frac{\partial V}{\partial u_{i\alpha}}\right)_{\mathbf{x}_0} = 0\right]$. Furthermore, under the harmonic approximation, the region of the PES surrounding $\mathbf{x}_0$ can be approximated as a harmonic potential—that is, all terms with third-order (or higher order) partial derivatives of the energy are neglected. With these considerations in mind, Eq. (A1) can be approximated as

$$V(\mathbf{x}) \approx \frac{1}{2!}\sum_{ij}^{N}\sum_{\alpha\beta}^{3}\left(\frac{\partial^2 V}{\partial u_{i\alpha}\partial u_{j\beta}}\right)_{\mathbf{x}_0} u_{i\alpha}u_{j\beta}. \tag{A2}$$

The partial derivative terms contained in Eq. (A2) constitute the elements of the $3N \times 3N$ Hessian matrix $\mathbf{H}$, with elements,

$$H_{i\alpha,j\beta} = \left(\frac{\partial^2 V}{\partial u_{i\alpha}\partial u_{j\beta}}\right)_{\mathbf{x}_0}. \tag{A3}$$

The mass-weighted Hessian $\mathbf{W}$ contains the elements,

$$W_{i\alpha,j\beta} = \frac{H_{i\alpha,j\beta}}{\sqrt{m_i m_j}} = \frac{1}{\sqrt{m_i m_j}}\left(\frac{\partial^2 V}{\partial u_{i\alpha}\partial u_{j\beta}}\right)_{\mathbf{x}_0}, \tag{A4}$$

where m_i, m_j refer to atomic masses, and this equation can be expressed in matrix form as

$$\mathbf{W} = \mathbf{M}^{-1/2}\mathbf{H}\mathbf{M}^{-1/2}, \tag{A5}$$

where $\mathbf{M}$ is a diagonal $3N \times 3N$ mass matrix with elements,

$$M_{i\alpha,j\beta} = \delta_{i\alpha,j\beta} m_i. \tag{A6}$$

In other words, $\mathbf{M}$ contains the atomic masses of each atom three times to account for the three Cartesian displacements of each atom (i.e., diagonal elements of $m_1, m_1, m_1, m_2, m_2, m_2, \ldots, m_N, m_N, m_N$). Once $\mathbf{W}$ has been computed, it can be diagonalized to obtain a set of eigenvalues and their corresponding eigenvectors,

$$\mathbf{C}^{\dagger}\mathbf{W}\mathbf{C} = \mathbf{\Lambda}, \tag{A7}$$

where the eigenvalues—squared angular frequencies $\{\omega_\mu^2\}$ ($\mu = 1, \ldots, 3N$)—are collected in the diagonal matrix $\mathbf{\Lambda}$, while the eigenvectors, which are column vectors, are collected in the matrix $\mathbf{C}$. Substituting the expression for $\mathbf{W}$ given by Eq. (A5) into Eq. (A7), we find that

$$\mathbf{C}^{\dagger}\mathbf{M}^{-1/2}\mathbf{H}\mathbf{M}^{-1/2}\mathbf{C} = \mathbf{\Lambda}, \tag{A8}$$

where $\mathbf{M}^{-1/2}\mathbf{C}$ and its adjoint $\mathbf{C}^{\dagger}\mathbf{M}^{-1/2}$ are shown. Quantum chemistry programs often express the eigenvectors collected by $\mathbf{C}$, which are dimensionless, in the mass-weighted form given by the matrix $\mathbf{M}^{-1/2}\mathbf{C} = \tilde{\mathbf{L}}$, where the tilde denotes mass weighting. Since the dimension of $\mathbf{M}$ is simply $[\mathbf{M}] = M$, where M is the dimension of mass, it follows that $[\tilde{\mathbf{L}}] = M^{-1/2}$, indicating that it is mass-weighted. Thus, Eq. (A8) can be alternatively expressed as

$$\tilde{\mathbf{L}}^{\dagger}\mathbf{H}\tilde{\mathbf{L}} = \mathbf{\Lambda}. \tag{A9}$$

In addition, $\tilde{\mathbf{L}}$ has the following property:

$$\tilde{\mathbf{L}}^{\dagger}\mathbf{M}\tilde{\mathbf{L}} = \mathbf{C}^{\dagger}\mathbf{M}^{-1/2}\mathbf{M}\mathbf{M}^{-1/2}\mathbf{C} = \mathbf{C}^{\dagger}\mathbf{C} = \mathbf{I}, \tag{A10}$$

since $\mathbf{C}$, being composed of the eigenvectors of the Hermitian $\mathbf{W}$ matrix, is a unitary matrix.

For an individual mass-weighted eigenvector $\tilde{\mathbf{l}}_\mu$, which represents a normal mode, its reduced mass m_μ^R can be expressed as

$$m_\mu^R = \frac{1}{\tilde{\mathbf{l}}_\mu^{\dagger}\tilde{\mathbf{l}}_\mu} = \frac{1}{\|\tilde{\mathbf{l}}_\mu\|^2}, \tag{A11}$$

with dimensions of $[m_\mu^R] = [\tilde{\mathbf{l}}_\mu]^{-2} = (M^{-1/2})^{-2} = M$. Equation (A11) indicates that $\|\tilde{\mathbf{l}}_\mu\| = (m_\mu^R)^{-1/2}$, so $\tilde{\mathbf{l}}_\mu$ can be renormalized as follows:

$$\mathbf{l}_\mu = \frac{\tilde{\mathbf{l}}_\mu}{\|\tilde{\mathbf{l}}_\mu\|} = (m_\mu^R)^{1/2}\tilde{\mathbf{l}}_\mu. \tag{A12}$$

Since $[m_\mu^R] = M$ and $[\tilde{\mathbf{l}}_\mu] = M^{-1/2}$, Eq. (A12) indicates that $\mathbf{l}_\mu$ is dimensionless and therefore mass-unweighted. These mass-unweighted eigenvectors can be collected in the matrix $\mathbf{L}$, and the reduced masses can be collected in the diagonal matrix $\mathbf{M}^R$. Hence, Eq. (A12) can be expressed in matrix form as

$$\mathbf{L} = \tilde{\mathbf{L}}(\mathbf{M}^R)^{1/2}, \tag{A13}$$

where $\mathbf{L}$ has two properties which are analogous to those of $\tilde{\mathbf{L}}$, which were given in Eqs. (A9) and (A10). The first property is observed when the mass-unweighted Hessian matrix $\mathbf{H}$ is diagonalized, yielding the eigenvectors collected in $\mathbf{L}$ as well as their corresponding eigenvalues collected in the diagonal matrix $\mathbf{K}$,

$$\mathbf{L}^{\dagger}\mathbf{H}\mathbf{L} = \mathbf{K}. \tag{A14}$$

Equations (A14) and (A9) can be utilized to evaluate the relationship between eigenvalue matrices $\mathbf{K}$ and $\mathbf{\Lambda}$. Multiplying both sides of Eq. (A9) by $(\mathbf{M}^R)^{1/2}$ (from the left and from the right), we obtain

$$\begin{aligned} \tilde{\mathbf{L}}^{\dagger}\mathbf{H}\tilde{\mathbf{L}} &= \mathbf{\Lambda}, \\ (\mathbf{M}^R)^{1/2}\tilde{\mathbf{L}}^{\dagger}\mathbf{H}\tilde{\mathbf{L}}(\mathbf{M}^R)^{1/2} &= (\mathbf{M}^R)^{1/2}\mathbf{\Lambda}(\mathbf{M}^R)^{1/2}, \\ \mathbf{L}^{\dagger}\mathbf{H}\mathbf{L} &= \mathbf{\Lambda}\mathbf{M}^R, \\ \mathbf{K} &= \mathbf{\Lambda}\mathbf{M}^R. \end{aligned} \tag{A15}$$

Equation (A15) indicates that the eigenvalues contained in $\mathbf{K}$ are given as $m_\mu^R(\omega_\mu^R)^2$. The second property of $\mathbf{L}$ can be obtained when both sides of Eq. (A10) are multiplied from the left and the right by $(\mathbf{M}^R)^{1/2}$,

$$\begin{gathered}\tilde{\mathbf{L}}^\dagger\mathbf{M}\tilde{\mathbf{L}} = \mathbf{I},\\ (\mathbf{M}^R)^{1/2}\tilde{\mathbf{L}}^\dagger\mathbf{M}\tilde{\mathbf{L}}(\mathbf{M}^R)^{1/2} = (\mathbf{M}^R)^{1/2}(\mathbf{M}^R)^{1/2},\\ \mathbf{L}^\dagger\mathbf{M}\mathbf{L} = \mathbf{M}^R.\end{gathered} \tag{A16}$$

To transform the $3N$ eigenvectors in $\mathbf{L}$, which are in Cartesian coordinates, into internal coordinates (e.g., bond lengths, bond angles, and dihedral angles), the $N_{vib} \times 3N$ Wilson $\mathbf{B}$ matrix[78,79] can be utilized. The elements of $\mathbf{B}$ are given as

$$\mathbf{B}_{n,i\alpha} = \frac{\delta q_n}{\delta u_{i\alpha}}, \tag{A17}$$

where q_n denotes the internal coordinate corresponding to the nth row of $\mathbf{B}$, $\mathbf{B}_n$. Thus, the eigenvectors of $\mathbf{L}$ can be expressed in internal coordinates as

$$\mathbf{D} = \mathbf{B}\mathbf{L}, \tag{A18}$$

where $\mathbf{D}$ collects these transformed eigenvectors as row vectors,

$$\mathbf{d}_n = \mathbf{B}_n\mathbf{L}. \tag{A19}$$

Like $\mathbf{L}$, $\mathbf{D}$ also has a mass-weighted analog, $\tilde{\mathbf{D}}$, which can be expressed as

$$\tilde{\mathbf{D}} = \mathbf{D}(\mathbf{M}^R)^{-1/2}, \tag{A20}$$

where each mass-weighted eigenvector can be expressed as

$$\tilde{\mathbf{d}}_n = \mathbf{d}_n(\mathbf{M}^R)^{-1/2}. \tag{A21}$$

In addition, the $\mathbf{B}$ matrix enables us to define the Wilson $\mathbf{G}$ matrix, given as

$$\mathbf{G} = \mathbf{B}\mathbf{M}^{-1}\mathbf{B}^\dagger, \tag{A22}$$

whose off-diagonal elements $G_{ij} = G_{ji}$ describe the kinetic energy coupling between any two modes i and j.[79] $\mathbf{G}$ can be alternatively expressed in terms of $\mathbf{D}$ using Eqs. (A18) and (A16), as shown below

$$\begin{aligned}\mathbf{G} &= \mathbf{B}\mathbf{M}^{-1}\mathbf{B}^\dagger\\ &= \mathbf{B}\mathbf{L}\mathbf{L}^{-1}\mathbf{M}^{-1}(\mathbf{L}^\dagger)^{-1}\mathbf{L}^\dagger\mathbf{B}^\dagger\\ &= \mathbf{D}(\mathbf{L}^\dagger\mathbf{M}\mathbf{L})^{-1}\mathbf{D}^\dagger\\ &= \mathbf{D}(\mathbf{M}^R)^{-1}\mathbf{D}^\dagger,\end{aligned} \tag{A23}$$

with diagonal elements,

$$\mathbf{G}_{nn} = \mathbf{d}_n(\mathbf{M}^R)^{-1}\mathbf{d}_n^\dagger. \tag{A24}$$

Once $\mathbf{L}$, $\mathbf{D}$, $\mathbf{M}^R$, $\mathbf{K}$, $\mathbf{\Lambda}$, and $\mathbf{G}$ are computed, then local vibrational modes and their properties can be obtained, as described in Appendix B.

APPENDIX B: PROPERTIES OF LOCAL VIBRATIONAL MODES

As mentioned in Sec. II A, each vector in $\{\mathbf{a}_n\}$, a set of local mode vectors associated with $\{q_n\}$, is expressed in normal coordinates as[80]

$$\mathbf{a}_n = \frac{\mathbf{K}^{-1}\mathbf{d}_n^\dagger}{\mathbf{d}_n\mathbf{K}^{-1}\mathbf{d}_n^\dagger}. \tag{B1}$$

Local mode vectors have three properties: local force constants, local masses, and local frequencies. For a given local mode vector $\mathbf{a}_n$, its associated local mode force constant k_n^a is expressed as[80,81]

$$k_n^a = \mathbf{a}_n^\dagger\mathbf{K}\mathbf{a}_n = \frac{1}{\mathbf{d}_n\mathbf{K}^{-1}\mathbf{d}_n^\dagger}, \tag{B2}$$

while its local mass, m_n^a, can be expressed as[80,81]

$$m_n^a = \frac{1}{G_{nn}} = [\mathbf{d}_n(\mathbf{M}^R)^{-1}\mathbf{d}_n^\dagger]^{-1}. \tag{B3}$$

Equations (B1) and (B2), which can be expressed in terms of $\mathbf{K}$ and $\mathbf{d}_n$, can also alternatively be expressed in terms of their counterparts $\mathbf{\Lambda}$ and $\tilde{\mathbf{d}}_n$ using Eqs. (A15) and (A21), respectively,

$$\mathbf{a}_n = (\mathbf{M}^R)^{-1/2}\frac{\mathbf{\Lambda}^{-1}\tilde{\mathbf{d}}_n^\dagger}{\tilde{\mathbf{d}}_n\mathbf{\Lambda}^{-1}\tilde{\mathbf{d}}_n^\dagger}, \tag{B4}$$

and

$$k_n^a = \mathbf{a}_n^\dagger\mathbf{\Lambda}\mathbf{M}^R\mathbf{a}_n = \frac{1}{\tilde{\mathbf{d}}_n\mathbf{\Lambda}^{-1}\tilde{\mathbf{d}}_n^\dagger}. \tag{B5}$$

Like k_n^a, m_n^a can also be directly expressed in terms of local modes. As a first step, we can rearrange Eq. (A15) to obtain $(\mathbf{M}^R)^{-1} = \mathbf{K}^{-1}\mathbf{\Lambda}$; it should be noted that $\mathbf{K}$, $\mathbf{\Lambda}$, and $\mathbf{M}^R$ can all commute with each other, since they are all diagonal matrices with the same dimensions. Substituting this expression for $(\mathbf{M}^R)^{-1}$ into Eq. (B3), we obtain

$$m_n^a = [(\mathbf{d}_n\mathbf{K}^{-1})(\mathbf{\Lambda}\mathbf{d}_n^\dagger)]^{-1}. \tag{B6}$$

The first term in parentheses, $\mathbf{d}_n\mathbf{K}^{-1}$, can expressed in terms of local modes and their force constants using Eqs. (B1) and (B2),

$$\begin{aligned}\mathbf{d}_n\mathbf{K}^{-1} &= [(\mathbf{K}^{-1})^\dagger\mathbf{d}_n^\dagger]^\dagger\\ &= [\mathbf{K}^{-1}\mathbf{d}_n^\dagger]^\dagger\\ &= [(k_n^a)^{-1}\mathbf{a}_n]^\dagger\\ &= (k_n^a)^{-1}\mathbf{a}_n^\dagger.\end{aligned} \tag{B7}$$

The second term in parentheses, $\mathbf{\Lambda}\mathbf{d}_n^\dagger$ can also be expressed in a similar manner using Eqs. (B4) and (B5),

$$\begin{aligned}\mathbf{\Lambda}\mathbf{d}_n^\dagger &= [\mathbf{\Lambda}\mathbf{I}][\mathbf{I}][\mathbf{I}\mathbf{d}_n^\dagger]\\ &= [\mathbf{\Lambda}(\mathbf{\Lambda}\mathbf{\Lambda}^{-1})][(\mathbf{M}^R)^{1/2}(\mathbf{M}^R)^{-1/2}][[(\mathbf{M}^R)^{1/2}(\mathbf{M}^R)^{-1/2}]\mathbf{d}_n^\dagger]\\ &= \mathbf{\Lambda}^2\mathbf{M}^R[(\mathbf{M}^R)^{-1/2}\mathbf{\Lambda}^{-1}\tilde{\mathbf{d}}_n^\dagger]\\ &= \mathbf{K}\mathbf{\Lambda}[(\mathbf{M}^R)^{-1/2}\mathbf{\Lambda}^{-1}\tilde{\mathbf{d}}_n^\dagger]\\ &= (k_n^a)^{-1}\mathbf{K}\mathbf{\Lambda}\mathbf{a}_n.\end{aligned} \tag{B8}$$

Substituting the expressions for the two terms into Eq. (B6), we obtain

$$m_n^a = \left[(k_n^a)^{-2}\mathbf{a}_n^\dagger \mathbf{K}\mathbf{\Lambda}\mathbf{a}_n\right]^{-1} = \frac{(k_n^a)^2}{\mathbf{a}_n^\dagger \mathbf{K}\mathbf{\Lambda}\mathbf{a}_n} = \frac{(\mathbf{a}_n^\dagger \mathbf{K}\mathbf{a}_n)^2}{\mathbf{a}_n^\dagger \mathbf{K}\mathbf{\Lambda}\mathbf{a}_n} = \frac{\langle \mathbf{a}_n|\mathbf{K}|\mathbf{a}_n\rangle^2}{\langle \mathbf{a}_n|\mathbf{K}\mathbf{\Lambda}|\mathbf{a}_n\rangle}, \tag{B9}$$

which can be alternatively expressed using Eq. (A15) as

$$m_n^a = \frac{\langle \mathbf{a}_n|\mathbf{\Lambda}\mathbf{M}^R|\mathbf{a}_n\rangle^2}{\langle \mathbf{a}_n|\mathbf{\Lambda}\mathbf{M}^R\mathbf{\Lambda}|\mathbf{a}_n\rangle}. \tag{B10}$$

Equations (B9) and (B10) provide a set of explicit relationships between local mode $\mathbf{a}_n$ and m_n^a. The latter of the two equations will be especially useful in our discussion of the mass weighting of local modes in Appendix C. Lastly, the local frequency of each local mode can be expressed (in cm^{-1}) as[72]

$$\omega_n^a = \frac{1}{2\pi c}\sqrt{\frac{k_n^a}{m_n^a}}, \tag{B11}$$

which, using Eqs. (B2) and (B9), can be re-expressed in terms of $\mathbf{a}_n$,

$$\omega_n^a = \frac{1}{2\pi c}\sqrt{\frac{\langle \mathbf{a}_n|\mathbf{K}\mathbf{\Lambda}|\mathbf{a}_n\rangle}{\langle \mathbf{a}_n|\mathbf{K}|\mathbf{a}_n\rangle}}. \tag{B12}$$

APPENDIX C: MASS WEIGHTING OF LOCAL VIBRATIONAL MODES

Here, we first apply dimensional analysis to $\mathbf{a}_n$ and $\mathbf{a}_n^x$. Based on this dimensional analysis, which indicates that the vectors are not mass-weighted, we will construct their mass-weighted analogs and evaluate their effects on the CNM procedure. M and L refer to dimensions of mass and length, respectively.

As previously mentioned in Appendix A, the $\mathbf{L}$ matrix is dimensionless. To evaluate the dimensions of $\mathbf{D}$, which collects the normal vectors in internal coordinates, we can consider the aforementioned relationship between $\mathbf{D}$ and $\mathbf{L}$,

$$\mathbf{D} = \mathbf{B}\mathbf{L}. \tag{C1}$$

For internal coordinate q_n, the corresponding $\mathbf{B}$ matrix elements are contained in $\mathbf{B}_n$, whose elements can be expressed as

$$\mathbf{B}_{n,i\alpha} = \frac{\delta q_n}{\delta u_{i\alpha}}. \tag{C2}$$

While q_n is dimensionless for bond angles and dihedral angles, $[q_n] = L$ for bonds. Therefore, given that $[u_{i\alpha}] = L$, $\mathbf{B}_n$ is dimensionless for bonds and $[\mathbf{B}_n] = L^{-1}$ for bond angles and dihedral angles.

As previously mentioned, $\mathbf{d}_n$ is given by

$$\mathbf{d}_n = \mathbf{B}_n\mathbf{L}. \tag{C3}$$

Since $\mathbf{L}$ is dimensionless, this expression for $\mathbf{d}_n$ indicates that $[\mathbf{d}_n] = [\mathbf{B}_n]$. Therefore, $\mathbf{d}_n$ is also dimensionless for bonds and $[\mathbf{d}_n] = L^{-1}$ for bond angles and dihedral angles.

The expression for a local mode vector $\mathbf{a}_n$, given by Eq. (1), indicates that $[\mathbf{a}_n] = [\mathbf{d}_n]^{-1}$. Therefore, $\mathbf{a}_n$ is dimensionless for bonds and $[\mathbf{a}_n] = L$ for bond angles and dihedrals. For all three types of internal coordinates, however, $\mathbf{a}_n$ does not involve mass as a dimension. Hence, $\mathbf{a}_n$ is not mass-weighted.

The linear transformation of $\mathbf{a}_n$ into $\mathbf{a}_n^x$ can be expressed as

$$\mathbf{a}_n^x = \mathbf{L}\mathbf{a}_n. \tag{C4}$$

Since $\mathbf{L}$ is dimensionless, $[\mathbf{a}_n^x] = [\mathbf{a}_n]$, so $\mathbf{a}_n^x$ is not mass-weighted either.

From Eq. (A12), we find that the transformation of a mass-unweighted normal mode to its mass-weighted counterpart is given as

$$\tilde{\mathbf{l}}_\mu = (m_\mu^R)^{-1/2}\mathbf{l}_\mu. \tag{C5}$$

Since $\mathbf{l}_\mu$ is dimensionless and $[(m_\mu^R)^{-1/2}] = M^{-1/2}$, it follows that $[\tilde{\mathbf{l}}_\mu] = M^{-1/2}$. The $M^{-1/2}$ dimension of $\tilde{\mathbf{l}}_\mu$ is indicative of its mass weighting. With this in mind, we can construct a mass-weighted local mode, defined as

$$\tilde{\mathbf{a}}_n = \zeta\mathbf{a}_n, \tag{C6}$$

where ζ is a scalar mass-weighting factor. Since $\mathbf{a}_n$ is dimensionless for bonds and $[\mathbf{a}_n] = L$ for angles, we will require the dimensions of $\tilde{\mathbf{a}}_n$ to be $[\tilde{\mathbf{a}}_n] = M^{-1/2}$ for bonds and $[\tilde{\mathbf{a}}_n] = M^{-1/2}L$ for angles. In this way, $\tilde{\mathbf{a}}_n$ includes an $M^{-1/2}$ dimensional term to account for mass-weighting, analogous to $\tilde{\mathbf{l}}_\mu$. With these dimensional constraints in mind, we find that the dimensions of ζ must be $[\zeta] = M^{-1/2}$.

Let ζ be defined as

$$\zeta = (m_n^a)^{-1/2}\|\mathbf{a}_n\| = (m_n^a)^{-1/2}\langle \mathbf{a}_n|\mathbf{a}_n\rangle^{1/2}. \tag{C7}$$

To evaluate the dimensions of this expression for ζ, we can first examine the expression for m_n^a given by Eq. (B10), which indicates that the dimensions of the local mass can be expressed as $[m_n^a] = [\mathbf{a}_n]^2[\mathbf{M}^R]$. Since $[\mathbf{M}^R] = M$, $\mathbf{a}_n$ is dimensionless for bonds, and $[\mathbf{a}_n] = L$ for bond angles and dihedral angles, the dimensions of m_n^a are $[m_n^a] = M$ for bonds and $[m_n^a] = ML^2$ for angles. In addition, $[\|\mathbf{a}_n\|] = [\langle \mathbf{a}_n|\mathbf{a}_n\rangle^{1/2}] = [\mathbf{a}_n]$. Thus, the dimensions of ζ are $[\zeta] = [(m_n^a)^{-1/2}\|\mathbf{a}_n\|] = [m_n^a]^{-1/2}[\mathbf{a}_n] = M^{-1/2}$ for all three internal coordinates, thereby satisfying its aforementioned dimensional requirement.

Substituting the expression for m_n^a [Eq. (B10)] into the expression for ζ [Eq. (C7)], we find that

$$\zeta = \left[\frac{\langle \mathbf{a}_n|\mathbf{\Lambda}\mathbf{M}^R\mathbf{\Lambda}|\mathbf{a}_n\rangle^{1/2}\langle \mathbf{a}_n|\mathbf{a}_n\rangle^{1/2}}{\langle \mathbf{a}_n|\mathbf{\Lambda}\mathbf{M}^R|\mathbf{a}_n\rangle}\right]. \tag{C8}$$

Substituting this expression for ζ into Eq. (C6), we obtain

$$\tilde{\mathbf{a}}_n = \mathbf{a}_n\left[\frac{\langle \mathbf{a}_n|\mathbf{\Lambda}\mathbf{M}^R\mathbf{\Lambda}|\mathbf{a}_n\rangle^{1/2}\langle \mathbf{a}_n|\mathbf{a}_n\rangle^{1/2}}{\langle \mathbf{a}_n|\mathbf{\Lambda}\mathbf{M}^R|\mathbf{a}_n\rangle}\right]. \tag{C9}$$

As previously mentioned, $\mathbf{a}_n^x = \mathbf{L}\mathbf{a}_n$. Since $\mathbf{L}$ is dimensionless, it follows that $[\mathbf{a}_n^x] = [\mathbf{a}_n]$. Therefore, we can consider a prescription analogous to Eq. (C6) for mass weighting $\mathbf{a}_n^x$,

$$\begin{aligned}\tilde{\mathbf{a}}_n^x &= \zeta \mathbf{a}_n^x \\ &= \zeta \mathbf{L}\mathbf{a}_n \\ &= \mathbf{L}(\zeta \mathbf{a}_n) \\ &= \mathbf{L}\tilde{\mathbf{a}}_n. \end{aligned} \tag{C10}$$

Since $\mathbf{L}$ is dimensionless, we observe from Eq. (C10) that $[\tilde{\mathbf{a}}_n^x] = [\tilde{\mathbf{a}}_n]$. Therefore, $\tilde{\mathbf{a}}_n^x$ is also mass-weighted. Substituting the expression for ζ given by Eq. (C8) into Eq. (C10), we find that

$$\tilde{\mathbf{a}}_n^x = \mathbf{a}_n^x \left[\frac{\langle \mathbf{a}_n | \boldsymbol{\Lambda}\mathbf{M}^R\boldsymbol{\Lambda} | \mathbf{a}_n \rangle^{1/2} \langle \mathbf{a}_n | \mathbf{a}_n \rangle^{1/2}}{\langle \mathbf{a}_n | \boldsymbol{\Lambda}\mathbf{M}^R | \mathbf{a}_n \rangle} \right]. \tag{C11}$$

We now assess the effects of mass weighting normal and local modes on the results of the CNM procedure. We can define $\tilde{S}_{n\mu}$, an analog of the $S_{n\mu}$ overlap term [Eq. (3)], which can be expressed as

$$\tilde{S}_{n\mu} = \frac{\langle \tilde{\mathbf{a}}_n^x | \mathbf{H} | \tilde{\mathbf{l}}_\mu \rangle^2}{\langle \tilde{\mathbf{a}}_n^x | \mathbf{H} | \tilde{\mathbf{a}}_n^x \rangle \langle \tilde{\mathbf{l}}_\mu | \mathbf{H} | \tilde{\mathbf{l}}_\mu \rangle}, \tag{C12}$$

which contains mass-weighted normal and local modes *in lieu* of their mass-unweighted counterparts. Equations (A12) and (C10) indicate that $|\tilde{\mathbf{l}}_\mu\rangle = (m_\mu^R)^{-1/2}|\mathbf{l}_\mu\rangle$ and $|\tilde{\mathbf{a}}_n^x\rangle = \zeta|\mathbf{a}_n^x\rangle$.

Therefore, $\tilde{S}_{n\mu}$ can be rewritten as

$$\begin{aligned}\tilde{S}_{n\mu} &= \frac{\langle \tilde{\mathbf{a}}_n^x | \mathbf{H} | \tilde{\mathbf{l}}_\mu \rangle^2}{\langle \tilde{\mathbf{a}}_n^x | \mathbf{H} | \tilde{\mathbf{a}}_n^x \rangle \langle \tilde{\mathbf{l}}_\mu | \mathbf{H} | \tilde{\mathbf{l}}_\mu \rangle} \\ &= \frac{\langle \mathbf{a}_n^x \zeta | \mathbf{H} | (m_\mu^R)^{-1/2} \mathbf{l}_\mu \rangle^2}{\langle \mathbf{a}_n^x \zeta | \mathbf{H} | \zeta \mathbf{a}_n^x \rangle \langle \mathbf{l}_\mu (m_\mu^R)^{-1/2} | \mathbf{H} | (m_\mu^R)^{-1/2} \mathbf{l}_\mu \rangle} \\ &= \frac{\langle \mathbf{a}_n^x | \mathbf{H} | \mathbf{l}_\mu \rangle^2}{\langle \mathbf{a}_n^x | \mathbf{H} | \mathbf{a}_n^x \rangle \langle \mathbf{l}_\mu | \mathbf{H} | \mathbf{l}_\mu \rangle} = S_{n\mu}. \end{aligned} \tag{C13}$$

Since $\tilde{S}_{n\mu} = S_{n\mu}$, mass weighting has no effect on the overlap between local and normal modes, so the CNM matrix $\mathbf{C}$, whose elements are given by Eq. (4), is not affected either. This result is of significance for the VCCA method, as discussed in Sec. II C.

REFERENCES

[1] F. C. Gillett, W. J. Forrest, and K. M. Merrill, Astrophys. J. **183**, 87 (1973).
[2] C. Moutou, K. Sellgren, L. Verstraete, and A. Léger, Astron. Astrophys. **347**, 949 (1999).
[3] L. Verstraete, J. L. Puget, E. Falgarone, S. Drapatz, C. M. Wright, and R. Timmermann, Astron. Astrophys. **315**, L337 (1996).
[4] R. Genzel, D. Lutz, E. Sturm, E. Egami, D. Kunze, A. F. M. Moorwood, D. Rigopoulou, H. W. W. Spoon, A. Sternberg, L. E. Tacconi-Garman, L. Tacconi, and N. Thatte, Astrophys. J. **498**, 579 (1998).
[5] S. Hony, C. Van Kerckhoven, E. Peeters, A. G. G. M. Tielens, D. M. Hudgins, and L. J. Allamandola, Astron. Astrophys. **370**, 1030 (2001).
[6] H. Andrews, C. Boersma, M. W. Werner, J. Livingston, L. J. Allamandola, and A. G. G. M. Tielens, Astrophys. J. **807**, 99 (2015).
[7] E. Peeters, S. Hony, C. Van Kerckhoven, A. G. G. M. Tielens, L. J. Allamandola, D. M. Hudgins, and C. W. Bauschlicher, Astron. Astrophys. **390**, 1089 (2002).
[8] B. Acke and M. E. van den Ancker, Astron. Astrophys. **426**, 151 (2004).
[9] J. Y. Seok and A. Li, Astrophys. J. **835**, 291 (2017).
[10] A. G. G. M. Tielens, Annu. Rev. Astron. Astrophys. **46**, 289 (2008).
[11] A. Li, Nat. Astron. **4**, 339 (2020).
[12] A. Leger and J. L. Puget, Astron. Astrophys. **137**, L5 (1984).
[13] H. R. Hrodmarsson, I. Aleman, A. Candian, S. Wiersma, J. Palotás, D. Dubois, A. Sidhu, D. Loru, P. Sundarajan, E. Sciamma-O'Brien, and A. G. G. M. Tielens, Space Sci. Rev. **221**, 42 (2025).
[14] L. J. Allamandola and A. G. G. M. Tielens, Astrophys. J. **290**, L25 (1985).
[15] L. J. Allamandola, A. G. G. M. Tielens, and J. R. Barker, Astrophys. J., Suppl. Ser. **71**, 733 (1989).
[16] D. J. Cook and R. J. Saykally, Astrophys. J. **493**, 793 (1998).
[17] C. Pech, C. Joblin, and P. Boissel, Astron. Astrophys. **388**, 639 (2002).
[18] M. Basire, P. Parneix, T. Pino, P. Bréchignac, and F. Calvo, in *EAS Publications Series*, edited by C. Joblin and A. Tielens (EDP, 2011), Vol. 46, pp. 95–101.
[19] C. J. Mackie, A. Candian, X. Huang, E. Maltseva, A. Petrignani, J. Oomens, W. J. Buma, T. J. Lee, and A. G. G. M. Tielens, J. Chem. Phys. **143**, 224314 (2015).
[20] C. J. Mackie, A. Candian, X. Huang, E. Maltseva, A. Petrignani, J. Oomens, W. J. Buma, T. J. Lee, and A. G. G. M. Tielens, Phys. Chem. Chem. Phys. **20**, 1189 (2018).
[21] C. J. Mackie, A. Candian, T. J. Lee, and A. G. G. M. Tielens, J. Phys. Chem. A **126**, 3198 (2022).
[22] B. A. McGuire, R. A. Loomis, A. M. Burkhardt, K. L. K. Lee, C. N. Shingledecker, S. B. Charnley, I. R. Cooke, M. A. Cordiner, E. Herbst, S. Kalenskii, M. A. Siebert, E. R. Willis, C. Xue, A. J. Remijan, and M. C. McCarthy, Science **371**, 1265 (2021).
[23] B. A. McGuire, A. M. Burkhardt, S. Kalenskii, C. N. Shingledecker, A. J. Remijan, E. Herbst, and M. C. McCarthy, Science **359**, 202 (2018).
[24] J. Cernicharo, M. Agúndez, C. Cabezas, B. Tercero, N. Marcelino, J. R. Pardo, and P. De Vicente, Astron. Astrophys. **649**, L15 (2021).
[25] A. M. Burkhardt, K. L. Lee, P. Changala, C. N. Shingledecker, I. R. Cooke, R. A. Loomis, H. Wei, S. B. Charnley, E. Herbst, M. C. McCarthy, and B. A. McGuire, Astrophys. J. Lett. **913**, L18 (2021).
[26] M. L. Sita, P. B. Changala, C. Xue, A. M. Burkhardt, C. N. Shingledecker, K. L. Kelvin Lee, R. A. Loomis, E. Momjian, M. A. Siebert, D. Gupta, E. Herbst, A. J. Remijan, M. C. McCarthy, I. R. Cooke, and B. A. McGuire, Astrophys. J. Lett. **938**, L12 (2022).
[27] J. Cernicharo, C. Cabezas, R. Fuentetaja, M. Agúndez, B. Tercero, J. Janeiro, M. Juanes, R. I. Kaiser, Y. Endo, A. L. Steber, D. Pérez, C. Pérez, A. Lesarri, N. Marcelino, and P. de Vicente, Astron. Astrophys. **690**, L13 (2024).
[28] G. Wenzel, I. R. Cooke, P. B. Changala, E. A. Bergin, S. Zhang, A. M. Burkhardt, A. N. Byrne, S. B. Charnley, M. A. Cordiner, M. Duffy, Z. T. P. Fried, H. Gupta, M. S. Holdren, A. Lipnicky, R. A. Loomis, H. T. Shay, C. N. Shingledecker, M. A. Siebert, D. A. Stewart, R. H. J. Willis, C. Xue, A. J. Remijan, A. E. Wendlandt, M. C. McCarthy, and B. A. McGuire, Science **386**, 810 (2024).
[29] G. Wenzel, T. H. Speak, P. B. Changala, R. H. Willis, A. M. Burkhardt, S. Zhang, E. A. Bergin, A. N. Byrne, S. B. Charnley, Z. T. Fried, H. Gupta, E. Herbst, M. S. Holdren, A. Lipnicky, R. A. Loomis, C. N. Shingledecker, C. Xue, A. J. Remijan, A. E. Wendlandt, M. C. McCarthy, I. R. Cooke, and B. A. McGuire, Nat. Astron. **9**, 262 (2025).
[30] G. Wenzel, S. Gong, C. Xue, P. B. Changala, M. S. Holdren, T. H. Speak, D. A. Stewart, Z. T. P. Fried, R. H. J. Willis, E. A. Bergin, A. M. Burkhardt, A. N. Byrne, S. B. Charnley, A. Lipnicky, R. A. Loomis, C. N. Shingledecker, I. R. Cooke, M. C. McCarthy, A. J. Remijan, A. E. Wendlandt, and B. A. McGuire, Astrophys. J. Lett. **984**, L36 (2025).
[31] J. Cernicharo, B. Tercero, N. Marcelino, J. A. López-Pérez, J. D. Gallego, F. Tercero, G. Esplugues, C. Cabezas, M. Agúndez, C. Limeres, A. L. Steber, D. Pérez, C. Pérez, A. Lesarri, and P. de Vicente, Astron. Astrophys. **705**, L7 (2026).
[32] R. Fuentetaja, C. Cabezas, M. Agúndez, B. Tercero, N. Marcelino, P. de Vicente, and J. Cernicharo, Astron. Astrophys. **706**, L10 (2026).
[33] H. Kim and R. J. Saykally, Astrophys. J., Suppl. Ser. **143**, 455 (2002).
[34] C. J. Mackie, A. Candian, T. J. Lee, and A. G. G. M. Tielens, Theor. Chem. Acc. **140**, 124 (2021).
[35] T. E. Douglas-Walker, E. K. Ashworth, M. H. Stockett, F. C. Daly, I. Chambrier, V. J. Esposito, M. Gerlach, A. Zheng, J. Palotás, A. N. Cammidge, E. K. Campbell, S. Brünken, and J. N. Bull, ACS Earth Space Chem. **9**, 134 (2025).
[36] M. H. Stockett, V. J. Esposito, E. K. Ashworth, U. Jacovella, and J. N. Bull, ACS Earth Space Chem. **9**, 382 (2025).

[37]D. J. Cook, S. Schlemmer, N. Balucani, D. R. Wagner, J. A. Harrison, B. Steiner, and R. J. Saykally, J. Phys. Chem. A **102**, 1465 (1998).
[38]S. Chakraborty, G. Mulas, M. Rapacioli, and C. Joblin, J. Mol. Spectrosc. **378**, 111466 (2021).
[39]I. Cherchneff and J. R. Barker, Astrophys. J. **341**, L21 (1989).
[40]O. Lacinbala, G. Féraud, J. Vincent, and T. Pino, J. Phys. Chem. A **126**, 4891 (2022).
[41]K. Li, A. Li, X. J. Yang, and T. Fang, Astrophys. J. **961**, 107 (2024).
[42]K. Li, A. Li, X. J. Yang, and T. Fang, Mon. Not. R. Astron. Soc. **529**, 4425 (2024).
[43]V. J. Esposito, P. Ferrari, W. J. Buma, R. C. Fortenberry, C. Boersma, A. Candian, and A. G. G. M. Tielens, J. Chem. Phys. **160**, 114312 (2024).
[44]C. J. Mackie, T. Chen, A. Candian, T. J. Lee, and A. G. G. M. Tielens, J. Chem. Phys. **149**, 134302 (2018).
[45]M. J. F. Rosenberg, O. Berné, and C. Boersma, Astron. Astrophys. **566**, L4 (2014).
[46]E. Peeters, C. W. Bauschlicher, L. J. Allamandola, A. G. G. M. Tielens, A. Ricca, and M. G. Wolfire, Astrophys. J. **836**, 198 (2017).
[47]A. Sidhu, E. Peeters, J. Cami, and C. Knight, Mon. Not. R. Astron. Soc. **500**, 177 (2021).
[48]B. A. Croiset, A. Candian, O. Berné, and A. G. G. M. Tielens, Astron. Astrophys. **590**, A26 (2016).
[49]C. Knight, E. Peeters, D. J. Stock, W. D. Vacca, and A. G. G. M. Tielens, Astrophys. J. **918**, 8 (2021).
[50]R. K. Anand, S. Rastogi, and B. Kumar, J. Astrophys. Astron. **44**, 47 (2023).
[51]C. W. Bauschlicher, Jr., E. Peeters, and L. J. Allamandola, Astrophys. J. **678**, 316 (2008).
[52]C. W. Bauschlicher, E. Peeters, and L. J. Allamandola, Astrophys. J. **697**, 311 (2009).
[53]A. Ricca, C. W. Bauschlicher, C. Boersma, A. G. G. M. Tielens, and L. J. Allamandola, Astrophys. J. **754**, 75 (2012).
[54]A. Candian, T. H. Kerr, I.-O. Song, J. McCombie, and P. J. Sarre, Mon. Not. R. Astron. Soc. **426**, 389 (2012).
[55]E. Peeters, L. Allamandola, C. Bauschlicher, Jr., D. Hudgins, S. Sandford, and A. Tielens, Astrophys. J. **604**, 252 (2004).
[56]D. M. Hudgins, C. Bauschlicher, Jr., and S. A. Sandford, Astrophys. J. **614**, 770 (2004).
[57]T. Onaka, T. I. Mori, I. Sakon, R. Ohsawa, H. Kaneda, Y. Okada, and M. Tanaka, Astrophys. J. **780**, 114 (2013).
[58]K. D. Doney, A. Candian, T. Mori, T. Onaka, and A. G. G. M. Tielens, Astron. Astrophys. **586**, A65 (2016).
[59]G. C. Sloan, M. Jura, W. W. Duley, K. E. Kraemer, J. Bernard-Salas, W. J. Forrest, B. Sargent, A. Li, D. J. Barry, C. J. Bohac, D. M. Watson, and J. R. Houck, Astrophys. J. **664**, 1144 (2007).
[60]X. J. Yang, R. Glaser, A. Li, and J. X. Zhong, Astrophys. J. **776**, 110 (2013).
[61]M. J. Shannon and C. Boersma, Astrophys. J. **871**, 124 (2019).
[62]L. J. Allamandola, C. Boersma, T. J. Lee, J. D. Bregman, and P. Temi, Astrophys. J. Lett. **917**, L35 (2021).
[63]X. Yang and A. Li, Astrophys. J., Suppl. Ser. **268**, 12 (2023).
[64]X. Yang and A. Li, Astrophys. J., Suppl. Ser. **268**, 50 (2023).
[65]Y. J. Pendleton and L. J. Allamandola, Astrophys. J., Suppl. Ser. **138**, 75 (2002).
[66]X. J. Yang, R. Glaser, A. Li, and J. X. Zhong, Mon. Not. R. Astron. Soc. **462**, 1551 (2016).
[67]X. J. Yang, R. Glaser, A. Li, and J. X. Zhong, New Astron. Rev. **77**, 1 (2017).
[68]X. J. Yang, A. Li, R. Glaser, and J. X. Zhong, Astrophys. J. **837**, 171 (2017).
[69]A. Ajaz, A. C. Voukides, K. J. Cahill, R. Thamatam, S. L. Skraba-Joiner, and R. P. Johnson, Aust. J. Chem. **67**, 1301 (2014).
[70]V. J. Esposito, S. Bejaoui, B. E. Billinghurst, C. Boersma, R. C. Fortenberry, and F. Salama, Mon. Not. R. Astron. Soc. **535**, 3239 (2024).
[71]E. Kraka, W. Zou, and Y. Tao, WIREs Comput. Mol. Sci. **10**, 1480 (2020).
[72]E. Kraka, M. Quintano, H. W. La Force, J. J. Antonio, and M. Freindorf, J. Phys. Chem. A **126**, 8781 (2022).
[73]I. M. Mills, *Molecular Spectroscopy: Modern Research* (Academic Press, 1972), pp. 115–140.
[74]J. K. G. Watson, *Vibrational Spectra and Structure* (Elsevier, 1977), pp. 1–89.
[75]R. C. Fortenberry and T. J. Lee, *Annual Reports in Computational Chemistry* (Elsevier, 2019), Vol. 15, pp. 173–202.
[76]P. R. Franke, J. F. Stanton, and G. E. Douberly, J. Phys. Chem. A **125**, 1301 (2021).
[77]R. C. Fortenberry and T. J. Lee, *Vibrational Dynamics of Molecules* (World Scientific, 2022), Vol. 1, p. 235.
[78]E. B. Wilson, Jr., J. Chem. Phys. **9**, 76 (1941).
[79]E. B. Wilson, Jr., J. C. Decius, and P. C. Cross, *Molecular Vibrations: The Theory of Infrared and Raman Vibrational Spectra* (McGraw-Hill, New York, 1955).
[80]Z. Konkoli and D. Cremer, Int. J. Quantum Chem. **67**, 1 (1998).
[81]Z. Konkoli, J. A. Larsson, and D. Cremer, Int. J. Quantum Chem. **67**, 11 (1998).
[82]Z. Konkoli and D. Cremer, Int. J. Quantum Chem. **67**, 29 (1998).
[83]Z. Konkoli, J. A. Larsson, and D. Cremer, Int. J. Quantum Chem. **67**, 41 (1998).
[84]N. Verma, Y. Tao, W. Zou, X. Chen, X. Chen, M. Freindorf, and E. Kraka, Sensors **20**, 2358 (2020).
[85]R. T. Moura, Jr., M. Quintano, J. J. Antonio, M. Freindorf, and E. Kraka, J. Phys. Chem. A **126**, 9313 (2022).
[86]M. J. Frisch, G. W. Trucks, H. B. Schlegel, G. E. Scuseria, M. A. Robb, J. R. Cheeseman, G. Scalmani, V. Barone, G. A. Petersson, H. Nakatsuji, X. Li, M. Caricato, A. V. Marenich, J. Bloino, B. G. Janesko, R. Gomperts, B. Mennucci, H. P. Hratchian, J. V. Ortiz, A. F. Izmaylov, J. L. Sonnenberg, D. Williams-Young, F. Ding, F. Lipparini, F. Egidi, J. Goings, B. Peng, A. Petrone, T. Henderson, D. Ranasinghe, V. G. Zakrzewski, J. Gao, N. Rega, G. Zheng, W. Liang, M. Hada, M. Ehara, K. Toyota, R. Fukuda, J. Hasegawa, M. Ishida, T. Nakajima, Y. Honda, O. Kitao, H. Nakai, T. Vreven, K. Throssell, J. A. Montgomery, Jr., J. E. Peralta, F. Ogliaro, M. J. Bearpark, J. J. Heyd, E. N. Brothers, K. N. Kudin, V. N. Staroverov, T. A. Keith, R. Kobayashi, J. Normand, K. Raghavachari, A. P. Rendell, J. C. Burant, S. S. Iyengar, J. Tomasi, M. Cossi, J. M. Millam, M. Klene, C. Adamo, R. Cammi, J. W. Ochterski, R. L. Martin, K. Morokuma, O. Farkas, J. B. Foresman, and D. J. Fox, *Gaussian 16 Revision C.01*, Gaussian Inc., Wallingford, CT, 2016.
[87]A. D. Becke, J. Chem. Phys. **98**, 5648 (1993).
[88]C. Lee, W. Yang, and R. G. Parr, Phys. Rev. B **37**, 785 (1988).
[89]V. Barone, P. Cimino, and E. Stendardo, J. Chem. Theory Comput. **4**, 751 (2008).
[90]V. Barone, M. Biczysko, and J. Bloino, Phys. Chem. Chem. Phys. **16**, 1759 (2014).
[91]R. C. Fortenberry, X. Huang, A. Yachmenev, W. Thiel, and T. J. Lee, Chem. Phys. Lett. **574**, 1 (2013).
[92]C. J. Mackie, A. Candian, X. Huang, T. J. Lee, and A. G. G. M. Tielens, J. Chem. Phys. **142**, 244107 (2015).
[93]J. F. Gaw, A. Willets, W. H. Green, and N. C. Handy, in *Advances in Molecular Vibrations and Collision Dynamics*, edited by J. Bowman and M. A. Ratner (JAI Press, 1991), p. 170.
[94]J. M. L. Martin and P. R. Taylor, Spectrochim. Acta, Part A **53**, 1039 (1997).
[95]J. M. L. Martin, T. J. Lee, P. R. Taylor, and J.-P. François, J. Chem. Phys. **103**, 2589 (1995).
[96]W. Zou, R. Moura, Jr., C. V. Santos, Jr., M. Quintano, F. Bodo, M. Freindorf, D. Cremer, and E. Kraka, *LModeA2025, Computational and Theoretical Chemistry Group (CATCO)* (Southern Methodist University, Dallas, TX, 2025).
[97]M. Quintano, R. T. Moura, Jr., and E. Kraka, Chem. Phys. Lett. **849**, 141416 (2024).
[98]N. Palanisamy and S. Banik, J. Phys. Chem. A **129**, 7794–7807 (2025).
[99]S. J. Goettl, A. M. Turner, V. S. Krasnoukhov, V. N. Azyazov, K. Kanayama, P. Hemberger, A. M. Mebel, and R. I. Kaiser, Sci. Adv. **11**, eadv0692 (2025).
[100]H. Lyu, P. Liu, T. Hu, Y. Song, J. Wan, K. Cheng, F. Zhou, X. Zhang, S. Lin, C. Zheng, W. L. Roberts, and X. Gao, J. Phys. Chem. A **129**, 6666 (2025).
[101]U. Çilesiz, E. Y. Sincer, B. Dedeoglu, and V. Aviyente, ACS Omega **10**, 23433 (2025).
[102]S. Mishra, A. Vats, S. Srivastav, A. Pathak, P. J. Sarre, T. Onaka, and I. Sakon, Mon. Not. R. Astron. Soc. **536**, 3357 (2025).
[103]V. Rawat, A. Shastri, A. K. Das, N. Sharma, H. Bhatt, and B. N. Rajasekhar, Spectrochim. Acta, Part A **324**, 124971 (2025).
[104]A. Omont and H. F. Bettinger, Astron. Astrophys. **696**, A180 (2025).

[105]M. Buragohain, T. Onaka, A. Pathak, A. Vats, and I. Sakon, Mon. Not. R. Astron. Soc. **538**, 3130 (2025).
[106]Y. Ge, C. Zhang, X. Hu, J. Liu, L. Qin, and J. Zhen, Astrophys. J., Suppl. Ser. **276**, 26 (2025).
[107]S. Haid, K. Gugeler, J. Kästner, and D. Campisi, Astron. Astrophys. **701**, A34 (2025).
[108]X. Wu, Y. Wu, L. Hua, X. Hu, N. Zhao, J. Zhen, and X. Yang, Mon. Not. R. Astron. Soc. **541**, 1241–1253 (2025).
[109]A. K. Lemmens, C. J. Mackie, A. Candian, T. M. J. Lee, A. G. G. M. Tielens, A. M. Rijs, and W. J. Buma, Faraday Discuss. **245**, 380 (2023).
[110]A. Maragkoudakis, E. Peeters, and A. Ricca, Mon. Not. R. Astron. Soc. **494**, 642 (2020).
[111]J. Wang, A. A. Nikolayev, J. H. Marks, A. M. Turner, S. Chandra, N. F. Kleimeier, L. A. Young, A. M. Mebel, and R. I. Kaiser, J. Am. Chem. Soc. **146**, 28437 (2024).
[112]M. Born and R. Oppenheimer, Ann. Phys. **389**, 457 (1927).